1 **SARS-CoV-2 ferritin nanoparticle vaccines elicit broad SARS coronavirus immunogenicity**
2
3
4 M. Gordon Joyce[1,2,12,]*, Wei-Hung Chen[1,2,], Rajeshwer S. Sankhala[1,2,], Agnes Hajduczki[1,2,], Paul V.
5 Thomas[1,2,], Misook Choe[1,2,], William Chang[1,2,], Caroline E. Peterson[1,2,], Elizabeth Martinez[1,2,], Elaine B.
6 Morrison[4], Clayton Smith[5,6], Aslaa Ahmed[7], Lindsay Wieczorek[2,4], Alexander Anderson[2,4], Rita E. Chen[3],
7 James Brett Case[3], Yifan Li[2,4], Therese Oertel[2,4], Lorean Rosado[2,4], Akshaya Ganesh[2,4], Connor Whalen[2,4],
8 Joshua M. Carmen[4], Letzibeth Mendez-Rivera[2,4], Christopher Karch[2,4], Neelakshi Gohain[2,4], Zuzana
9 Villar[2,4], David McCurdy[2,4], Zoltan Beck[2,4], Jiae Kim[2,4], Shikha Shrivastava[2,4], Ousman Jobe[2,4], Vincent
10 Dussupt[2,4], Sebastian Molnar[2,4], Ursula Tran[2,4], Chandrika B. Kannadka[2,4], Michelle Zemil[2,4], Htet Khanh[5,6],
11 Weimin Wu[5,6], Matthew A. Cole[8], Debra K. Duso[8], Larry W. Kummer[8], Tricia J. Lang[8], Shania E. Muncil[8],
12 Jeffrey R. Currier[7], Shelly J. Krebs[2,4], Victoria R. Polonis[4], Saravanan Rajan[9], Patrick M. McTamney[10],
13 Mark T. Esser[10], William W. Reiley[8], Morgane Rolland[2,4], Natalia de Val[5,6], Michael S. Diamond[3], Gregory
14 D. Gromowski[7], Gary R. Matyas[4], Mangala Rao[4], Nelson L. Michael[11], and Kayvon Modjarrad[1,]*
15
16 1. Emerging Infectious Diseases Branch, Walter Reed Army Institute of Research, Silver Spring, MD,
17   USA.
18 2. Henry M. Jackson Foundation for the Advancement of Military Medicine, Bethesda, MD, USA.
19 3. Department of Medicine, Washington University School of Medicine, St. Louis, MO 63110, USA;
20   Department of Pathology & Immunology, Washington University School of Medicine, St. Louis, MO
21   63110, USA; Department of Molecular Microbiology, Washington University School of Medicine,
22   St. Louis, MO 63110, USA; The Andrew M. and Jane M. Bursky Center for Human Immunology &
23   Immunotherapy Programs, Washington University School of Medicine, St. Louis, MO 63110, USA.
24 4. U.S. Military HIV Research Program, Walter Reed Army Institute of Research, Silver Spring, MD,
25   USA.
26 5. Center for Molecular Microscopy, Center for Cancer Research, National Cancer Institute, National
27   Institutes of Health, Frederick, MD, USA.
28 6. Cancer Research Technology Program, Frederick National Laboratory for Cancer Research, Leidos
29   Biomedical Research Inc., Frederick, MD, USA.
30 7. Viral Diseases Branch, Walter Reed Army Institute of Research, Silver Spring, MD, USA.
31 8. Trudeau Institute, Inc., Saranac Lake, NY, USA.
32 9. Antibody Discovery and Protein Engineering (ADPE), BioPharmaceuticals R&D, AstraZeneca,
33   Gaithersburg, USA
34 10. Microbial Sciences, BioPharmaceuticals R&D, AstraZeneca, Gaithersburg, MD, USA.
35 11. Center for Infectious Diseases Research, Walter Reed Army Institute of Research, Silver Spring, MD,
36   USA.
37 12. Lead contact
38
39 *Correspondence: gjoyce@eidresearch.org (MGJ), kayvon.modjarrad.civ@mail.mil (KM)

SUMMARY

The need for SARS-CoV-2 next-generation vaccines has been highlighted by the rise of variants of concern (VoC) and the long-term threat of other coronaviruses. Here, we designed and characterized four categories of engineered nanoparticle immunogens that recapitulate the structural and antigenic properties of prefusion Spike (S), S1 and RBD. These immunogens induced robust S-binding, ACE2-inhibition, and authentic and pseudovirus neutralizing antibodies against SARS-CoV-2 in mice. A Spike-ferritin nanoparticle (SpFN) vaccine elicited neutralizing titers more than 20-fold higher than convalescent donor serum, following a single immunization, while RBD-Ferritin nanoparticle (RFN) immunogens elicited similar responses after two immunizations. Passive transfer of IgG purified from SpFN- or RFN-immunized mice protected K18-hACE2 transgenic mice from a lethal SARS-CoV-2 virus challenge. Furthermore, SpFN- and RFN-immunization elicited ACE2 blocking activity and neutralizing ID50 antibody titers >2,000 against SARS-CoV-1, along with high magnitude neutralizing titers against major VoC. These results provide design strategies for pan-coronavirus vaccine development.

Keywords: SARS-CoV-2, ferritin nanoparticle, Spike, receptor binding domain, COVID-19, SARS-CoV-1, β-coronaviruses, variants of concern, B.1.1.7, B.1.351, P.1, ALFQ, neutralizing antibodies

HIGHLIGHTS

- Iterative structure-based design of four Spike-domain Ferritin nanoparticle classes of immunogens
- SpFN-ALFQ and RFN-ALFQ immunization elicits potent neutralizing activity against SARS-CoV-2, variants of concern, and SARS-CoV-1
- Passively transferred IgG from immunized C57BL/6 mice protects K18-hACE2 mice from lethal SARS-CoV-2 challenge

INTRODUCTION

Seven coronaviruses (CoV) cause disease in humans, with three of these, SARS-CoV-1, MERS-CoV, and SARS-CoV-2 having emerged since 2003 (Cui et al., 2019) and displaying high mortality rates. SARS-CoV-2 is easily transmitted by humans and created a pandemic, infecting over 100 million people, causing over 2 million deaths to date, and resulting in an urgent need for protective and durable vaccines. Rapid vaccine development in a worldwide effort, led to the evaluation of hundreds of SARS-CoV-2 vaccine candidates and rapid worldwide vaccine distribution and use.

The response to SARS-CoV-2 was facilitated by multiple efforts over the last decade to enable CoV pandemic preparedness, initially based on MERS-CoV vaccine design and development (Wang et al., 2015), phase I vaccine trials (Modjarrad et al., 2019), and a global effort by the Coalition for Epidemic Preparedness Innovations (CEPI) to advance vaccine candidates (Plotkin, 2017). The elucidation of CoV Spike (S) glycoprotein structures (Kirchdoerfer et al., 2016; Walls et al., 2016) allowed structure-based vaccine design of stabilized S glycoprotein immunogens from multiple CoVs (Pallesen et al., 2017), providing a blueprint for SARS-CoV-2 vaccine design (Corbett et al., 2020).

The CoV S protein mediates virus entry, is immunogenic (Iyer et al., 2020; Wang et al., 2021) and encodes multiple neutralizing epitopes (Greaney et al., 2021) making it the primary target for natural and vaccine-induced CoV humoral immunity and vaccine design (Jiang et al., 2020) and the target of most COVID-19 vaccines. S is a class I fusion glycoprotein consisting of a S1 attachment subunit and S2 fusion subunit that remain non-covalently associated in a metastable, heterotrimeric S on the virion surface (Walls et al., 2020). In the S1 subunit, there is a N-terminal domain (NTD), and C-terminal domain (CTD) that includes the receptor-binding domain (RBD). The RBD binds to the human angiotensin converting enzyme 2 (hACE2) facilitating cell entry (Lan et al., 2020). Multiple antigenic sites have been identified on the S protein, including distinct sites on the RBD and the S1 domain, including an NTD supersite (Brouwer et al., 2020; Cerutti et al., 2021; Liu et al., 2020; Zost et al., 2020). Convalescent serum antibodies or monoclonal antibodies capable of potently inhibiting infection *in vitro* can reduce disease severity or mortality in rodents, non-human primates (Barnes et al., 2020) and humans (Duan et al., 2020; Salazar et al., 2020; Shen et al., 2020).

Due to the unknown parameters of SARS-CoV-2 vaccine durability, specific age- or population-needs, emergence of SARS-CoV-2 variants of concern (VoC) (Wibmer et al., 2020), and the constant threat of emerging CoV pathogens (Menachery et al., 2015), second-generation COVID-19 or pan-sarbecovirus vaccines will be needed. Iterative structure-based design for viral glycoproteins (McLellan et al., 2013; Joyce et al., 2016) stabilizing neutralizing epitopes or epitope-based vaccine design (Chen et al., 2021; Kong et al., 2019) show that rational vaccine design can lead to the elicitation of broad immune responses. Broad cross-reactive responses elicited by engineered vaccines have also been advanced for influenza (Boyoglu-Barnum et al., 2020; Kanekiyo et al., 2019). In the case of CoVs, a set of cross-reactive epitopes have recently been described (Barnes et al., 2020; Joyce et al., 2020; Sauer et al., 2021; Wrapp et al., 2020), with many of the preferred neutralizing antibodies centered on the RBD domain (Li et al., 2021; Pinto et al., 2020; Rappazzo et al., 2021).

Next-generation strategies to augment specific immune responses as well as enhance cross-reactivity include the use of nanoparticle vaccine technology (Cohen et al., 2021) and next-generation adjuvants. Nanoparticle technologies have been shown to improve antigen

structure and stability, as well as vaccine targeted delivery, immunogenicity, with good safety profiles (Pati et al., 2018). Engineered nanoparticle-vaccines can elicit broader immune responses (Darricarrere et al., 2021; Kanekiyo et al., 2019; Kanekiyo et al., 2013) or more efficacious immune responses (Kanekiyo et al., 2015). The repetitive array of the viral surface component allows for robust B-cell activation facilitating memory B cell expansion and generation of long-lived plasma cells. More recently, in efforts to generate more effective vaccines that can prevent infection by resistant pathogens such as HIV-1 or Influenza, a set of engineered nanoparticle vaccines have been developed. Utilizing naturally occurring nanoparticle molecules such as bacterial ferritin, antigens are fused to the ferritin molecule to recapitulate complex trimeric class I glycoproteins, and to increase the immune response for weakly immunogenic targets. Nanoparticle technologies have also been shown to improve antigen structure and stability, as well as vaccine targeted delivery, immunogenicity and safety (Pati et al., 2018). Recently designed single and multi-component nanoparticle vaccines (Brouwer et al., 2021; Walls et al., 2020) show promise from both an immunological (Cawlfield et al., 2019; Marcandalli et al., 2019) and a cGMP production perspective (Ueda et al., 2020).

Engineered nanoparticle vaccines and their capacity to generate enhanced immune responses in humans are currently being studied and include influenza (NCT03186781; NCT03814720; NCT04579250), Epstein-Barr virus (NCT04645147), malaria (NCT04296279) and a recently described SARS-CoV-2 nanoparticle vaccine (IVX-411) (Walls et al., 2020). Use of potent adjuvants such as liposomal-saponin adjuvants can further enhance the protective immune response (Cawlfield et al., 2019; Lal et al., 2015; Om et al., 2020) even in the context of nanoparticle vaccines (Langowski et al., 2020) (Kaba et al., 2018). Based on the results described herein and data from associated non-human primate experiments (Joyce et al., 2021; King et al., 2021), a S-Ferritin immunogen with a liposomal adjuvant, ALFQ is currently being assessed in a phase I clinical trial (NCT04784767).

Here we report the structure-based design and pre-clinical assessment of four categories of S-domain ferritin nanoparticles including stabilized S-trimer-ferritin nanoparticles (SpFN), RBD-ferritin nanoparticles (RFN), S1-ferritin nanoparticles, and RBD-NTD-ferritin nanoparticles. By using a set of biophysical, structural, and antigenic assessments, combined with animal immunogenicity testing, we identify multiple immunogens that elicit substantial neutralizing antibody titers against SARS-CoV-2 and related VoC. These antibody levels provide robust protection against SARS-CoV-2 challenge in the K18-hACE2 mouse model. We further show that subsequent immunizations not only increase the SARS-CoV-2 neutralization titer, but also expand the neutralization breadth and titer against the heterologous SARS-CoV-1 virus. These data provide multiple immunogen design strategies for pan-betacoronavirus vaccine development.

RESULTS

Immunogen Design of SARS-CoV-2 S-domain Ferritin Nanoparticles

Using the initial SARS-CoV-2 genome sequence (Genbank: MN9089473), we designed four categories of S-domain ferritin-fusion recombinant proteins as immunogens for expression as nanoparticles based on the major antigenic domains of the S ectodomain (Figure S1). The *Helicobacter pylori* ferritin molecule was genetically linked to the C-terminal region of the

163 following S antigens (i) S ectodomain (residues 12-1158) (ii) RBD (residues 331-527), (iii)
164 RBD linked in tandem to the NTD (residues 12-303), and (iv) S1 (residues 12-696) (Figure
165 1, Figure S1, and Table S1). In the case of the Spike ferritin nanoparticle designs, a short
166 linker to the ferritin molecule was used to utilize the natural three-fold axis, for display of
167 eight Spikes. In the case of the other designs, a short region of bullfrog ferritin was utilized
168 to allow equidistant distribution of the 24 S-domain molecules on the ferritin surface (Figure
169 1). Our overall approach was to compare and contrast the immunogen structures,
170 antigenicity, immunogenicity elicited by these different immunogens with the goal to
171 identify the best immunogen to take forward into further development.
172   The first design category, Spike ferritin nanoparticle designs were based on a
173 modified S with stabilizing prolines (K986P, V987P), removal of the furin cleavage site (RRAS
174 to GSAS), and optimization of the coiled coil region between hinge 1 and hinge 2 of the
175 ectodomain stalk (Turonova et al., 2020) to stabilize trimer formation on the Ferritin scaffold
176 (Figure 1A and S1). The designs focused on (i) modification of the end of the S molecule
177 (1137, 1208, 1154, or 1158), (ii) optimization of the coiled-coil region through extensions or
178 repeats, (iii) removal of the coiled-coil region, (iv) removal of glycan 1158, (v) addition of
179 heterogenous trimerization domains (GCN4, or foldon), or (vi) signal peptide sequence
180 (Figure 1B, and Table S1).
181   The second design category, RBD ferritin nanoparticle designs used the SARS-CoV-2
182 RBD (residues 331-527) (Figure 1C) connected to the bullfrog-H. pylori chimeric ferritin
183 (Kanekiyo et al., 2015) by a 6 amino acid linker (Figure 1D). The SARS-CoV-2 RBD contains
184 a set of hydrophobic patches, including the ACE2 binding site, and a region located about
185 residue 518 that is covered in the context of the intact S molecule. These regions were
186 iteratively mutated to reduce hydrophobicity, and increase stability of the RFN molecules,
187 expression levels, and antigenicity and immunogenicity.
188   The third design category, RBD-NTD ferritin molecules were based on addition of
189 optimized RBD molecules in series with an NTD-Ferritin construct (residues 12-303) linked
190 to the bullfrog-H. pylori chimeric ferritin molecule. The in-series, but reversed RBD-NTD
191 design ensured distal displacement of the RBD molecule from the ferritin molecule (Figure
192 1E), promoting immune recognition of the RBD molecule with potential benefits for the
193 production and stability of the nanoparticle.
194   The fourth design category, S1 ferritin design SARS-CoV-2 S (residues 12 - 676)
195 (Figure 1F, and Table S1) was initially designed based on the MERS S1 immunogen which
196 elicited protective immune responses (Wang et al., 2015). Subsequent designs focused on
197 inclusion of a short region of SARS-CoV-2 S2 (residues 689-696) either using the connecting
198 region that overlaps with the furin site, or by use of a short glycine-rich linker sequence
199 (Figure 1F) to enable formation of the S1-Ferritin nanoparticle (Figure 1G).
200
201 **Characterization of SARS-CoV-2 S-domain ferritin nanoparticles**
202
203 Ten S-ferritin constructs (Table S1) were initially designed and tested for expression, yield,
204 nanoparticle formation, and antigenicity. S-ferritin nanoparticles were expressed in
205 Expi293F cells for 3-5 days at 34 °C and 37 °C and purified by GNA lectin affinity
206 chromatography. A subset of these constructs showed reasonable expression levels ranging
207 from 0.5 to 5 mg/L media supernatant (Figure S3). pCoV1B-05 and pCoV1B-06-PL (SpFN)
208 typically yielded over 5 mg/L with expression incubation set at 34 °C. Samples were

209   assessed by SDS-PAGE, size-exclusion chromatography (SEC), dynamic light scattering
210   (DLS), and negative-stain electron microscopy (neg-EM) to ensure intact protein was
211   produced, and to assess the nanoparticle formation, and S morphology (Figure 2 and . For
212   all SpFN constructs that showed expression as visualized by SDS-PAGE (Figure 2A),
213   nanoparticles were observed by SEC, DLS, and neg-EM (Figure 2E, and 2F). In the case of
214   SpFN and SpFN_1B-08 (Figure S2), the globular shape of the protruding S was clearly
215   visible in both the TEM images and the 2D averages. In the case of the pCoV1B-05, the
216   protruding S showed more of an "open" form in both the TEM images and the 2D averages.
217   Nanoparticles were assessed for nanoparticle formation, and assessed for
218   antigenicity using biolayer interferometry against a set of poorly neutralizing (CR3022,
219   SR1), and potently neutralizing (SR2, SR3, SR4, SR5) RBD-targeting antibodies. The
220   different S-ferritin designs showed variable binding to the antibodies, with SpFN having
221   the highest binding (Figure 3A and Figure S1).
222   Initial test expression of RBD-Ferritin constructs at 37 ^{o}C using either 293F or
223   Expi293F cells showed low levels of expression. Reducing the cell expression temperature
224   to between 30 ^{o}C to 34 ^{o}C following transfection rescued expression and enabled levels >
225   20 mg/L to be purified by NiNTA purification (Figure S3). However, analysis of the
226   constructs by SEC, DLS, and neg-EM indicated that initial RBD-Ferritin constructs did not
227   form fully intact nanoparticles (Figure S2). We hypothesized that designed variants with
228   reduced RBD surface hydrophobicity would allow for improved nanoparticle yield.
229   Screening through a set of variants using SDS-PAGE and SEC as primary indicators of
230   nanoparticle formation allowed identification of constructs that readily formed
231   nanoparticles (Figure 2 and Figure S1 and S2B). These molecules were also visualized by
232   neg-EM, and showed clear formation of nanoparticles, with the protruding RBD domain
233   visible on their surface in both TEM images and 2D class averages (Figure 2F). However,
234   these constructs had a propensity to form soluble or insoluble aggregates and dramatically
235   affected the ability to concentrate the samples. Addition of 5% glycerol to the NiNTA
236   purified material, prior to SEC or other concentration steps, mitigated the aggregation issue
237   and increased the nanoparticle formation as judged by SEC, and was confirmed by neg-EM.
238   The RBD-Ferritin constructs showed very strong binding to the set of RBD-specific
239   antibodies in all cases (Figure S3E). The level of binding was approximately twice that seen
240   for the S-ferritin constructs, indicative of the exposed and accessible nature of the RBD
241   epitopes (Figure 2G).
242   Due to the initial difficulty with S1-Ferritin nanoparticle constructs, we developed a
243   set of engineered S1 constructs by artificially connecting the RBD domain by a short linker
244   to NTD linked to the Ferritin molecule and denoted as RBD-NTD ferritin molecules. This
245   multi-domain strategy resulted in good expression and nanoparticle formation. Using the
246   information gained from the RBD surface optimization, we designed multiple constructs
247   with variations in the RBD molecule to reduce surface hydrophobicity (Figure S1).
248   Antigenic analysis of these constructs showed that pCoV146 displayed robust antibody-
249   binding (Figure 2F).
250   The initial S1-Ferritin construct, pCoV68 (residues 12-676) yielded very low protein
251   expression levels, even with reduced expression temperatures(Figure S3A). However,
252   using the structure of the S-2P molecule (Wrapp et al., 2020; Walls et al., 2020), it was clear
253   that a short segment of the S2 formed significant interactions with the S1 domain. Addition
254   of this short region either using the natural sequence (with furin site removed) as in

6

255   construct pCoV109, or by linking residues 689-696 with glycine-rich linkers as in construct
256   pCoV111 allowed ~ 1 mg/L of protein to be purified. Analysis of these constructs by SDS-
257   PAGE, SEC, and neg-EM showed clear formation of the designed nanoparticles, and
258   antigenic characterization showed binding of antibodies to the nanoparticle (Figure 2G).
259   Further structural analysis of the nanoparticle immunogens from each of the four
260   design categories was carried out by determining 3D reconstructions from negative-stain
261   electron micrographs (Figure 4). For each nanoparticle, a central sphere of approximately
262   12 nm corresponding to ferritin was resolved. S-domain antigens were located a short
263   distance away from the central sphere and linker regions were unresolved likely due to
264   their small size and flexibility. The SpFN_1B-06-PL reconstruction showed the stabilized S
265   protruding from the ferritin molecule with a total diameter of approximately 44 nm (Figure
266   4A). The large size and distinct low-resolution features of the S ectodomain allowed for
267   docking of a closed S-2P trimer model (PDB ID: 6VXX) into the trimer density, confirming
268   the S was in the prefusion conformation. The ferritin-distal region of the S density was
269   slightly weaker and likely reflects the heterogeneity in RBD-up conformations or slight
270   openings of trimer visible in raw micrographs. Additionally, although the coiled-coil was
271   unresolved, the distances between the density for S and ferritin matched the modeled
272   coiled-coil length. Reconstruction of the three-dimensional RFN_131 EM map revealed two
273   globular densities per asymmetric unit, suggesting that the RBD molecule was highly
274   flexible on the surface of the ferritin sphere (Figure 4B). Similarly, the map of the RBD-
275   NTD-ferritin fusion, pCoV146, showed two layers of globular densities, with a ferritin-
276   proximal layer corresponding to the NTD domain and a more disordered layer for the RBD
277   domain (Figure 4C). This particle was approximately 9nm larger in 2D and 3D than the
278   single domain RFN molecule. The reconstruction of the S1-Ferritin fusion pCoV111
279   revealed a surprisingly ordered S1 density compared to the flexible RBD-NTD fusion,
280   perhaps due to geometric constraints on the surface of the ferritin particle (Figure 4D). A
281   density similar in shape to the S1 domain in the closed S2P trimer was resolved although it
282   was slightly more compact, likely due to both overall flexibility of the S1 on the ferritin
283   surface and RBD flexibility.
284

285   **Immunogenicity of the four categories of SARS-CoV-2 S-domain ferritin nanoparticles**
286   **in mice**
287

288   To evaluate the immunogenicity of the SARS-CoV-2 ferritin-nanoparticles, we typically
289   utilized two strains of mice (C57BL/6, and BALB/c), two adjuvants (ALFQ, and Alhydrogel®),
290   and immunized mice three-times intramuscularly at 3-week intervals using a 10 μg dose. In
291   total, we assessed 14 immunogens, two Spike ferritin immunogens, seven RBD ferritin
292   immunogens, one S1-Ferritin construct, and four RBD-NTD ferritin immunogens (Table S2).
293   Assessment in immunogenicity studies was based on iterative knowledge of immunogen
294   physical and biochemical characteristics (Figure 2 and 3, and Figure S3), in conjunction with
295   immunogenicity results from first-generation immunogens (Figure S1). This facilitated
296   down-selection of lead immunogen candidates. Alhydrogel® and ALFQ adjuvants were
297   selected due to their history in human vaccine trials, safety profile, and previous
298   performance alongside nanoparticle vaccine immunogens (NCT04296279). Alhydrogel®
299   contains aluminum hydroxide gel, while ALFQ is a liposome-based adjuvant containing the

300   saponin QS-21, and synthetic Monophosphoryl Lipid A (3D-PHAD®). We assessed SARS-CoV-
301   2 RBD- and S-binding, RBD-ACE2-inhibition, pseudovirus neutralizing antibody responses
302   and authentic SARS-CoV-2 virus neutralization (Figure 4).
303   All four categories of immunogens elicited robust SARS-CoV-2 immune responses. In
304   all cases tested, ALFQ was superior to Alhydrogel® as an adjuvant for elicitation of binding
305   and neutralizing responses (Figure S4). In addition, Alhydrogel® led to a skewed antibody
306   isotype immune response that was TH2 in nature, as opposed to the balanced immune
307   response seen with ALFQ adjuvanted animals (Figure S4G). Immune responses seen in
308   C57BL/6 mice were greater than for BALB/c mice after a single immunization, while binding
309   and neutralizing antibody titers were comparable after a second or third immunization
310   (Figure 5). In all cases, the third immunization did not dramatically increase the antibody
311   levels induced by the S-domain ferritin nanoparticles.
312   The SpFN immunogen elicited a rapid RBD-binding, and pseudovirus neutralizing
313   antibody response with ID_{50} geometric mean titer (GMT) >10,000 in C57BL/6 mice and
314   >1,000 after a single immunization (Figure 5C and Figure S4). This rapid neutralizing
315   immune response after one immunization was significantly higher than seen with RBD
316   ferritin or RBD-NTD ferritin immunogens. Following a second immunization, both strains of
317   SpFN-vaccinated mice showed ID_{50} GMT >10,000 and ID_{80} GMT >5,000 for both mouse types.
318   RBD ferritin immunogens elicited robust RBD and S-binding responses, ACE2-
319   inhibition, and pseudovirus neutralization ID50 GMT >10,000 in both mice strains after two
320   immunizations (Figure 5A-C). We assessed seven RFN immunogen designs in
321   immunogenicity studies (Table S3) and selection for animal immunogenicity experiments
322   was largely based on nanoparticle stability, expression levels, aggregation, and antigenic
323   profile (Figure 2-3 and Figure S2, S3). Based on these criteria, pCoV131 (RFN) was
324   extensively assessed, and after three immunizations, showed pseudovirus neutralization
325   responses that were comparable or exceeded that seen for the SpFN_1B-06-PL immunogen.
326   Of note, the RFN immunogens elicited substantial S binding responses that were highly
327   comparable to that of other immunogens that contained additional S domains (Figure 5B).
328   In a pattern similar to that seen for the RBD ferritin immunogens, both the RBD-NTD
329   ferritin and the S1 ferritin immunogens elicited binding responses, and detectable
330   pseudovirus neutralization after a single immunization that were increased by the second
331   immunization to give ID_{50} GMT values >10,000, and ID_{80} GMT titers ~5,000 (Figure 5A-C and
332   Figure S4).
333   Given the rapid elicitation of immune responses after a single immunization by
334   SpFN_1B-06-PL, we further characterized this immunogen in a dose-ranging study (Figure
335   S5 and Figure 5D and 5E). In five-fold dilution steps, we reduced the SpFN_1B-06-PL
336   immunogen from a 10 µg dose down to a 0.0032 µg dose (3,125-fold reduction) with the full
337   ALFQ adjuvant dose. Antibody binding responses were assessed for the full dose range by
338   ELISA to S and RBD, and binding responses were elicited at all dose concentrations tested.
339   We then further assessed the 0.08 µg dose (125-fold reduction from the 10 µg dose) with all
340   our immunogenicity assays (Figure 5D and Figure S5G). At this dose, the immune response
341   was comparable to that seen for the typical 10 µg dose. In addition, we assessed both the 10
342   and 0.08 µg SpFN_1B-06-PL vaccinated-mouse serum for authentic SARS-CoV-2 live virus
343   neutralization. At both doses, in both mouse strains, a single immunization elicited ID_{50} GMT
344   of ~ 1,000, while the second immunization boosted this response more than ten-fold. The

345 subsequent third immunization showed a modest boost effect. At each of these study time
346 points, there was no difference between the doses in C57BL/6 mice, while differences in
347 BALB/c ID80 GMT were seen at week 2 (higher for the 10 µg dose) and week 8 (higher for
348 the 0.08 µg dose). Overall, these studies demonstrated robust immunogenicity of four
349 categories of SARS-CoV-2 S-domain ferritin nanoparticles.
350
351 **Protective Immunity in K18-hACE2 transgenic mice against SARS-CoV-2 Challenge**
352
353 Given the neutralizing antibody response seen with SpFN, and RFN, and the different
354 design of these two immunogens, we chose to assess antibodies from these animals in a
355 lethal SARS-CoV-2 challenge model using K18-hACE2 transgenic mice. The dose of SARS-
356 CoV-2 virus was titrated to establish significant weight loss and pathology following
357 infection with WA strain (Figure S6). Given previously described studies (Zheng et al.,
358 2021), we sought to assess the vaccine-elicited antibody responses at levels starting at
359 about 1,000 and we passively transferred three different amounts of purified IgG from
360 either SpFN- or RFN-immunized mice 24 h prior to infection with SARS-CoV-2 (Figure 6A,
361 6B). The control groups included a PBS group and a group that was passively transferred
362 with naïve mouse IgG.
363   Animal weight was measured twice daily for 14 days after challenge, and animals
364 that lost > 25% weight during the study were euthanized. All animals that received the
365 highest amount of antibody (470 µg SpFN-derived, or 370 µg RFN-derived) showed
366 neutralization ID_{50} GMT titers of 1,713 and 1,179 respectively (Figure 6C). All animals in
367 these two groups showed minimal weight loss (Figure 6D), and all animals survived the
368 study (Figure 6E). In the two groups that received either 47 µg SpFN- or 37 µg RFN-derived
369 antibody, neutralization ID_{50} GMT titers were 89, and 248 respectively. Even with these
370 modest antibody transfer amounts and the relatively low neutralization titers, most
371 animals were protected from weight loss and death. In the SpFN-47 µg group, only two
372 animals showed severe weight loss, while in the RFN-37 µg group, most animals showed
373 some weight loss during the first study week, but all recovered. In contrast, mice that
374 received the lowest amount of purified IgG from SpFN- or RFN-vaccinated animals, did not
375 show any neutralizing antibody titers at the day of infection. The mice in these two groups
376 showed significant weight loss, and 9/10 animals in each group were euthanized by day 9
377 of the study. In a similar pattern, all animals from the naïve IgG and PBS groups suffered
378 weight loss and were euthanized by study day 8. In summary, these data show that low
379 amounts of passively transferred antibodies from SpFN or RFN vaccinated animals can
380 protect mice from a lethal challenge with SARS-CoV-2.
381
382 **Vaccine-elicited broadly cross-reactive antibody responses against SARS-CoV-1 and**
383 **SARS-CoV-2**
384
385 SARS-CoV-2 variants that are more transmissible and appear to be more lethal continue to
386 emerge even in the midst of rapid vaccine roll out and public-health measures. Given the
387 robust binding, pseudovirus and authentic virus neutralization titers against the original
388 SARS-CoV-2, that were elicited by the S-domain ferritin nanoparticle immunogens, we
389 assessed the immunized mouse sera for binding and pseudovirus neutralization to the VoC
390 (Figure 7). Using study week 10 sera from mice immunized with the four categories of

9

391 immunogens SpFN_1B-06-PL, RFN_131, pCoV146, and pCoV111 (S1-Ferritin), we assessed
392 binding to a panel of variant RBD molecules containing K417N, E484K, N501Y, and
393 combinations of these mutations (Figure 7A). These mutations match to the RBD sequence
394 seen in the B.1.351, B.1.1.7, and P.1 SARS-CoV-2 strains. In all cases, robust binding to the
395 RBD molecules were observed, with minimal change in overall binding when compared to
396 the original RBD molecule. RFN-immunized mouse sera showed reduced binding to the
397 E484K, N501Y double mutant, but increased binding to the K417N variant. Analysis of the
398 sera from SpFN-, RFN, or pCoV111-immunized mice for pseudovirus neutralization of VoCs
399 B.1.1.7 and B.1.351 showed minimal changes in the neutralization levels, with ID_{50} values >
400 2,000 for all strains (Figure 7B).
401   Analysis of the mouse sera for binding or neutralization of SARS-CoV-1 showed that
402 RFN-immunized mice elicited the highest SARS-CoV-1 RBD binding response (Figure 7C).
403 In addition, to RBD binding, we also observed SARS-CoV-1 ACE2-RBD inhibitory activity
404 with the SpFN-immunized mice (Figure S5). We further assessed the SpFN- or RFN-
405 immunized mouse sera for neutralization against SARS-CoV-1 using the pseudovirus assay
406 (Figure 7D). We observed robust neutralization levels with ID_{50} > 1,000 for the
407 SpFN_1B06-PL or the RFN_131 immunized animals. In general, the RFN molecule elicited
408 higher SARS-CoV-1 neutralizing responses compared to the SpFN-immunized animals.
409 Together, these data demonstrate that the S-domain ferritin nanoparticles elicit broadly
410 neutralizing and cross-reactive antibody responses against VoC and heterologous SARS-
411 CoV-1.
412
413 **DISCUSSION**
414
415 Since the emergence of SARS-CoV-2 in late 2019, multiple vaccines have been developed that
416 elicit robust and protective immune responses in small animals, non-human primates, and
417 humans. This includes a set of mRNA-based vaccines (NIH-Moderna Pfizer-BioNTech), viral
418 vector vaccines (J&J, Astra Zeneca), and a nanoparticle-like vaccine (Novavax) (Bangaru et
419 al., 2020) that are starting to be distributed worldwide, and include SARS-CoV-2 S as the
420 major vaccine component. In addition, next generation SARS-CoV-2 vaccine candidates are
421 beginning to reveal strong immunological results in pre-clinical studies (Saunders et al.,
422 2021; Walls et al., 2020). These protein-based nanoparticle platforms paired with powerful
423 adjuvant systems provide multiple advantages in the ability to protect against emerging
424 variants (Moyo-Gwete et al., 2021; Wibmer et al., 2021). Nanoparticle vaccines may be
425 critical for specific high-risk professions, or in populations where immune response titers
426 are of particular importance (Atyeo et al., 2021) including the elderly (Collier et al., 2021) or
427 immunocompromised (Boyarsky et al., 2021). The utility of highly stable vaccines that can
428 elicit high neutralizing antibody titers after a single immunization, or vaccines that can be
429 easily re-purposed for specific populations or as boosting immunogens is likely to help the
430 long-term strategy for global COVID-19 vaccination.
431   Trimer-functionalized ferritin vaccines have been effective at eliciting neutralizing
432 antibodies against class I fusion proteins, including influenza haemagglutinin (Kanekiyo et
433 al., 2013; Kelly et al., 2020) and HIV envelope (He et al., 2016; Sliepen et al., 2015) as well as
434 engineered nanoparticles including RBD-12GS-I53-50 (Walls et al., 2020). For example, in
435 the case of respiratory syncytial virus, a stabilized prefusion Fusion glycoprotein vaccine
436 based on subtype A can naturally elicit potent neutralizing antibody and T cell responses

437 against the heterologous subtype B in animals and humans (Crank et al., 2019; Joyce et al.,
438 2019). Here we developed a set of SARS-CoV-2 S-domain ferritin nanoparticle vaccines using
439 structure-based vaccine design that recreate the structural and antigenic profile of S. These
440 immunogens elicit antibodies with potent S-binding activity, hACE2-blocking activity, and
441 potent neutralization activity against the homologous virus. In all four immunogen-design
442 groups, antibody responses target the RBD domain and this response significantly
443 contributes to the high neutralization responses. Additionally, dose-sparing immunization
444 experiments show that significant antigen reduction can still elicit potent antibody
445 responses, while simultaneously also showing robust levels of neutralizing antibodies
446 against the heterologous SARS-CoV-1. This heterologous immune response is reminiscent of
447 broad immune responses seen with Ferritin-HA immunogens (Kanekiyo et al., 2013), and
448 demonstrate how nanoparticle immunogens can enhance the quality of the humoral immune
449 response. Naturally occurring nanoparticle vaccines such as Yellow Fever 17D vaccine
450 (Collins and Barrett, 2017) and human papillomavirus virus-like particle (VLP) vaccines
451 (Lowy and Schiller, 2006) elicit robust and long-lived immune responses. For SARS-CoV-2
452 vaccine development, nanoparticles performed well in mouse (Keech et al., 2020; Walls et
453 al., 2020) and non-human primate studies (Brouwer et al., 2021), with a designed S-Ferritin
454 nanoparticle also resulting in robust immunogenicity in mouse studies (Powell et al., 2021).
455 Furthermore, the passive-transfer of vaccine-elicited purified antibody prevented
456 death and significant weight loss in a high-dose SARS-CoV-2 challenge in the K18-hACE2
457 mouse model at neutralizing antibody levels that were routinely exceeded by SpFN- or RFN-
458 vaccination. We also transferred very low amounts of antibody to the K18-hACE2 mice to
459 assess for antibody dependent enhancement, and we saw no indication of faster weight loss,
460 or enhanced symptoms in the mice. The fact that antibody amounts readily elicited after a
461 single immunization are highly protective in this challenge model, and that low antibody
462 levels do not enhance disease, highlights the promise of these vaccine candidates. A set of
463 companion papers also maps out the cellular immune response and highlights the protective
464 effect of SpFN and RFN in high-dose SARS-CoV-2 challenge studies (Joyce et al., 2021; King
465 et al., 2021). Given the rapid elicitation of SARS-CoV-2 immune responses after a single
466 immunization and the highly protective responses seen in the K18-hACE2 model, SpFN_1B-
467 06-PL has been produced under current Good Manufacturing Practice (cGMP) conditions
468 and is under assessment in an ongoing phase I clinical trial (NCT04784767).
469 The immune responses elicited by the ferritin nanoparticles with the adjuvant ALFQ
470 were consistently superior to that seen with the aluminum hydroxidebased Alhydrogel
471 adjuvant. This result is consistent with other studies indicating that aluminum hydroxide is
472 sub-optimal at inducing SARS-COV-2 neutralizing antibody responses [ref]. The
473 components of the ALFQ adjuvant including QS-21, are used in multiple industrial
474 processes and scaled up for future advanced clinical trials. The COVID-19 pandemic has set
475 many precedents in regard to vaccine development speed, novel platforms, and should
476 garner a new age of vaccine development utilizing advanced antigens and adjuvants to
477 train the immune response for increased protection.
478 Here, we utilized structure-based design to create four categories of immunogens using the
479 ferritin-nanoparticle platform. Each of these different designs and the underlying
480 development processes provide a greater understanding and framework for ongoing and
481 future pan-coronavirus vaccine design and development. The design information outlined
482 here can be readily transferred for emerging CoV pathogens or other ubiquitous "common-

483   cold" coronaviruses. The utilization of the SARS-CoV-2 nanoparticle immunogen provided
484   immunogenicity against variants of concern and the heterologous SARS-CoV-1 and has
485   implications for vaccination efforts against putative zoonotic emergences.

AUTHOR CONTRIBUTIONS

M.G.J. and K.M. designed the study. M.G.J., P.V.T., and K.M. designed the immunogens. M.G.J., W-H.C., M.C., R.S.S., A.H., P.V.T., R.E.C. W.C.C., C.E.P., E.J.M., E.M., A.A., C.S., J.B.C., Y.L., A.A., J.K., T.O., L.R., A.G., C.W., J.C., L.M.-R., C.K., N.G., Z.V., D.McC., Z.B., J.K., S.S., O.J., V.D., S.M., U.T., C.B.K., M.Z., H.K., W.W., M.A.C., D.K.D., L.W.K., T.J.L., S.E.M., S.J.K., S.M., V.R.P., W.W.R., N.deV., M.S.D., G.D.G., and M.Rao performed protein purification, biophysical assays, immunologic assays and animal studies. Z.B., M.Rao, G.R.M., and A.And. designed and provided the adjuvants. S.R., P.M.M. and M.T.E. provided the SR1-5 antibodies. M.G.J., W.H.C., R.S.S., A.H., P.V.T., R.E.C., C.S., A.Ahm., L.W., Z.B., W.W., W.W.R., M.Ro., N.deV., M.S.D., G.D.G., M.Rao, N.L.M. and K.M. analyzed and interpreted the data. M.G.J. wrote the paper with assistance from all coauthors.

DECLARATIONS OF INTERESTS

M.G.J. and K.M. are named as inventors on International Patent Application No. WO/2021/21405 entitled "Vaccines against SARS-CoV-2 and other coronaviruses." M.G.J. is named as an inventor on International Patent Application No. WO/2018/081318 and U.S. patent 10,960,070 entitled "Prefusion Coronavirus Spike Proteins and Their Use." Z.B. is named as an inventor on U.S. patent 10,434,167 entitled "Non-toxic adjuvant formulation comprising a monophosphoryl lipid A (MPLA)-containing liposome composition and a saponin." Z.B. and G.R.M are named inventors on "Compositions And Methods For Vaccine Delivery", US Patent Application: 16/607,917. M.S.D. is a consultant for Inbios, Vir Biotechnology, NGM Biopharmaceuticals and Carnival Corporation and on the Scientific Advisory Boards of Moderna and Immunome. The Diamond laboratory has received funding support in sponsored research agreements from Moderna, Vir Biotechnology and Emergent BioSolutions. S.R., P.M.M., and M.T.E. are employees of AstraZeneca and currently hold AstraZeneca stock or stock options. Zoltan Beck is currently employed at Pfizer.

REFERENCES

Bangaru, S., Ozorowski, G., Turner, H.L., Antanasijevic, A., Huang, D., Wang, X., Torres, J.L., Diedrich, J.K., Tian, J.H., Portnoff, A.D., *et al.* (2020). Structural analysis of full-length SARS-CoV-2 spike protein from an advanced vaccine candidate. Science *370*, 1089-1094.

Barnes, C.O., West, A.P., Jr., Huey-Tubman, K.E., Hoffmann, M.A.G., Sharaf, N.G., Hoffman, P.R., Koranda, N., Gristick, H.B., Gaebler, C., Muecksch, F., *et al.* (2020). Structures of Human Antibodies Bound to SARS-CoV-2 Spike Reveal Common Epitopes and Recurrent Features of Antibodies. Cell *182*, 828-842 e816.

Boyarsky, B.J., Werbel, W.A., Avery, R.K., Tobian, A.A.R., Massie, A.B., Segev, D.L., and Garonzik-Wang, J.M. (2021). Immunogenicity of a Single Dose of SARS-CoV-2 Messenger RNA Vaccine in Solid Organ Transplant Recipients. JAMA.

Boyington, J.C., Joyce, M.G., Sastry, M., Stewart-Jones, G.B., Chen, M., Kong, W.P., Ngwuta, J.O., Thomas, P.V., Tsybovsky, Y., Yang, Y., *et al.* (2016). Structure-Based Design of Head-Only Fusion Glycoprotein Immunogens for Respiratory Syncytial Virus. PLoS One *11*, e0159709.

Boyoglu-Barnum, S., Ellis, D., Gillespie, R.A., Hutchinson, G.B., Park, Y.-J., Moin, S.M., Acton, O., Ravichandran, R., Murphy, M., Pettie, D., *et al.* (2020). Elicitation of broadly protective immunity to influenza by multivalent hemagglutinin nanoparticle vaccines. bioRxiv, 2020.2005.2030.125179.

Brouwer, P.J.M., Brinkkemper, M., Maisonnasse, P., Dereuddre-Bosquet, N., Grobben, M., Claireaux, M., de Gast, M., Marlin, R., Chesnais, V., Diry, S., *et al.* (2021). Two-component spike nanoparticle vaccine protects macaques from SARS-CoV-2 infection. Cell *184*, 1188-1200 e1119.

Brouwer, P.J.M., Caniels, T.G., van der Straten, K., Snitselaar, J.L., Aldon, Y., Bangaru, S., Torres, J.L., Okba, N.M.A., Claireaux, M., Kerster, G., *et al.* (2020). Potent neutralizing antibodies from COVID-19 patients define multiple targets of vulnerability. Science *369*, 643-650.

Case, J.B., Rothlauf, P.W., Chen, R.E., Liu, Z., Zhao, H., Kim, A.S., Bloyet, L.M., Zeng, Q., Tahan, S., Droit, L., *et al.* (2020). Neutralizing Antibody and Soluble ACE2 Inhibition of a Replication-Competent VSV-SARS-CoV-2 and a Clinical Isolate of SARS-CoV-2. Cell Host Microbe *28*, 475-485 e475.

Cawlfield, A., Genito, C.J., Beck, Z., Bergmann-Leitner, E.S., Bitzer, A.A., Soto, K., Zou, X., Hadiwidjojo, S.H., Gerbasi, R.V., Mullins, A.B., *et al.* (2019). Safety, toxicity and immunogenicity of a malaria vaccine based on the circumsporozoite protein (FMP013) with the adjuvant army liposome formulation containing QS21 (ALFQ). Vaccine *37*, 3793-3803.

Cerutti, G., Guo, Y., Zhou, T., Gorman, J., Lee, M., Rapp, M., Reddem, E.R., Yu, J., Bahna, F., Bimela, J., *et al.* (2021). Potent SARS-CoV-2 neutralizing antibodies directed against spike N-terminal domain target a single supersite. Cell Host Microbe.

Chen, X., Zhou, T., Schmidt, S.D., Duan, H., Cheng, C., Chuang, G.Y., Gu, Y., Louder, M.K., Lin, B.C., Shen, C.H., *et al.* (2021). Vaccination induces maturation in a mouse model of diverse unmutated VRC01-class precursors to HIV-neutralizing antibodies with >50% breadth. Immunity *54*, 324-339 e328.

Cohen, A.A., Gnanapragasam, P.N.P., Lee, Y.E., Hoffman, P.R., Ou, S., Kakutani, L.M., Keeffe, J.R., Wu, H.J., Howarth, M., West, A.P., *et al.* (2021). Mosaic nanoparticles elicit cross-reactive immune responses to zoonotic coronaviruses in mice. Science *371*, 735-741.

576   Collier, D.A., Ferreira, I.A.T.M., Datir, R., Meng, B., Bergamaschi, L., Elmer, A., Kingston, N.,
577   Graves, B., Smith, K.G., Bradley, J.R., *et al.* (2021). Age-related heterogeneity in Neutralising
578   antibody responses to SARS-CoV-2 following BNT162b2 vaccination. medRxiv,
579   2021.2002.2003.21251054.
580   Collins, N.D., and Barrett, A.D. (2017). Live Attenuated Yellow Fever 17D Vaccine: A Legacy
581   Vaccine Still Controlling Outbreaks In Modern Day. Curr Infect Dis Rep *19*, 14.
582   Corbett, K.S., Edwards, D.K., Leist, S.R., Abiona, O.M., Boyoglu-Barnum, S., Gillespie, R.A.,
583   Himansu, S., Schafer, A., Ziwawo, C.T., DiPiazza, A.T., *et al.* (2020). SARS-CoV-2 mRNA
584   vaccine design enabled by prototype pathogen preparedness. Nature *586*, 567-571.
585   Crank, M.C., Ruckwardt, T.J., Chen, M., Morabito, K.M., Phung, E., Costner, P.J., Holman, L.A.,
586   Hickman, S.P., Berkowitz, N.M., Gordon, I.J., *et al.* (2019). A proof of concept for structure-
587   based vaccine design targeting RSV in humans. Science *365*, 505-509.
588   Cui, J., Li, F., and Shi, Z.L. (2019). Origin and evolution of pathogenic coronaviruses. Nat Rev
589   Microbiol *17*, 181-192.
590   Darricarrere, N., Qiu, Y., Kanekiyo, M., Creanga, A., Gillespie, R.A., Moin, S.M., Saleh, J.,
591   Sancho, J., Chou, T.H., Zhou, Y., *et al.* (2021). Broad neutralization of H1 and H3 viruses by
592   adjuvanted influenza HA stem vaccines in nonhuman primates. Sci Transl Med *13*.
593   Duan, K., Liu, B., Li, C., Zhang, H., Yu, T., Qu, J., Zhou, M., Chen, L., Meng, S., Hu, Y., *et al.*
594   (2020). Effectiveness of convalescent plasma therapy in severe COVID-19 patients. Proc
595   Natl Acad Sci U S A *117*, 9490-9496.
596   Greaney, A.J., Starr, T.N., Gilchuk, P., Zost, S.J., Binshtein, E., Loes, A.N., Hilton, S.K.,
597   Huddleston, J., Eguia, R., Crawford, K.H.D., *et al.* (2021). Complete Mapping of Mutations to
598   the SARS-CoV-2 Spike Receptor-Binding Domain that Escape Antibody Recognition. Cell
599   Host Microbe *29*, 44-57 e49.
600   Iyer, A.S., Jones, F.K., Nodoushani, A., Kelly, M., Becker, M., Slater, D., Mills, R., Teng, E.,
601   Kamruzzaman, M., Garcia-Beltran, W.F., *et al.* (2020). Dynamics and significance of the
602   antibody response to SARS-CoV-2 infection. medRxiv.
603   Jiang, S., Hillyer, C., and Du, L. (2020). Neutralizing Antibodies against SARS-CoV-2 and
604   Other Human Coronaviruses. Trends Immunol *41*, 355-359.
605   Joyce, M.G., Bao, A., Chen, M., Georgiev, I.S., Ou, L., Bylund, T., Druz, A., Kong, W.P., Peng, D.,
606   Rundlet, E.J., *et al.* (2019). Crystal Structure and Immunogenicity of the DS-Cav1-Stabilized
607   Fusion Glycoprotein From Respiratory Syncytial Virus Subtype B. Pathog Immun *4*, 294-
608   323.
609   Joyce, M.G., King, H.A.D., Elakhal Naouar, I., Ahmed, A., Peachman, K.K., Cincotta, C.M., Subra,
610   C., Chen, R.E., Thomas, P.V., Chen, W.-H., *et al.* (2021). Efficacy of a Broadly Neutralizing
611   SARS-CoV-2 Ferritin Nanoparticle Vaccine in Nonhuman Primates. bioRxiv,
612   2021.2003.2024.436523.
613   Joyce, M.G., Sankhala, R.S., Chen, W.H., Choe, M., Bai, H., Hajduczki, A., Yan, L., Sterling, S.L.,
614   Peterson, C.E., Green, E.C., *et al.* (2020). A Cryptic Site of Vulnerability on the Receptor
615   Binding Domain of the SARS-CoV-2 Spike Glycoprotein. bioRxiv.
616   Kaba, S.A., Karch, C.P., Seth, L., Ferlez, K.M.B., Storme, C.K., Pesavento, D.M., Laughlin, P.Y.,
617   Bergmann-Leitner, E.S., Burkhard, P., and Lanar, D.E. (2018). Self-assembling protein
618   nanoparticles with built-in flagellin domains increases protective efficacy of a Plasmodium
619   falciparum based vaccine. Vaccine *36*, 906-914.

620 Kanekiyo, M., Bu, W., Joyce, M.G., Meng, G., Whittle, J.R., Baxa, U., Yamamoto, T., Narpala, S.,
621 Todd, J.P., Rao, S.S., *et al.* (2015). Rational Design of an Epstein-Barr Virus Vaccine Targeting
622 the Receptor-Binding Site. Cell *162*, 1090-1100.
623 Kanekiyo, M., Joyce, M.G., Gillespie, R.A., Gallagher, J.R., Andrews, S.F., Yassine, H.M.,
624 Wheatley, A.K., Fisher, B.E., Ambrozak, D.R., Creanga, A., *et al.* (2019). Mosaic nanoparticle
625 display of diverse influenza virus hemagglutinins elicits broad B cell responses. Nat
626 Immunol *20*, 362-372.
627 Kanekiyo, M., Wei, C.J., Yassine, H.M., McTamney, P.M., Boyington, J.C., Whittle, J.R., Rao, S.S.,
628 Kong, W.P., Wang, L., and Nabel, G.J. (2013). Self-assembling influenza nanoparticle
629 vaccines elicit broadly neutralizing H1N1 antibodies. Nature *499*, 102-106.
630 Keech, C., Albert, G., Cho, I., Robertson, A., Reed, P., Neal, S., Plested, J.S., Zhu, M., Cloney-
631 Clark, S., Zhou, H., *et al.* (2020). Phase 1-2 Trial of a SARS-CoV-2 Recombinant Spike Protein
632 Nanoparticle Vaccine. N Engl J Med *383*, 2320-2332.
633 King, H.A.D., Gordon Joyce, M., Naouar, I.E., Ahmed, A., Cincotta, C.M., Subra, C., Peachman,
634 K.K., Hack, H.H., Chen, R.E., Thomas, P.V., *et al.* (2021). Efficacy and breadth of adjuvanted
635 SARS-CoV-2 receptor-binding domain nanoparticle vaccine in macaques. bioRxiv,
636 2021.2004.2009.439166.
637 Kirchdoerfer, R.N., Cottrell, C.A., Wang, N., Pallesen, J., Yassine, H.M., Turner, H.L., Corbett,
638 K.S., Graham, B.S., McLellan, J.S., and Ward, A.B. (2016). Pre-fusion structure of a human
639 coronavirus spike protein. Nature *531*, 118-121.
640 Kong, R., Duan, H., Sheng, Z., Xu, K., Acharya, P., Chen, X., Cheng, C., Dingens, A.S., Gorman, J.,
641 Sastry, M., *et al.* (2019). Antibody Lineages with Vaccine-Induced Antigen-Binding Hotspots
642 Develop Broad HIV Neutralization. Cell *178*, 567-584 e519.
643 Lal, H., Cunningham, A.L., Godeaux, O., Chlibek, R., Diez-Domingo, J., Hwang, S.J., Levin, M.J.,
644 McElhaney, J.E., Poder, A., Puig-Barbera, J., *et al.* (2015). Efficacy of an adjuvanted herpes
645 zoster subunit vaccine in older adults. N Engl J Med *372*, 2087-2096.
646 Lan, J., Ge, J., Yu, J., Shan, S., Zhou, H., Fan, S., Zhang, Q., Shi, X., Wang, Q., Zhang, L., *et al.*
647 (2020). Structure of the SARS-CoV-2 spike receptor-binding domain bound to the ACE2
648 receptor. Nature *581*, 215-220.
649 Langowski, M.D., Khan, F.A., Bitzer, A.A., Genito, C.J., Schrader, A.J., Martin, M.L., Soto, K., Zou,
650 X., Hadiwidjojo, S., Beck, Z., *et al.* (2020). Optimization of a Plasmodium falciparum
651 circumsporozoite protein repeat vaccine using the tobacco mosaic virus platform. Proc Natl
652 Acad Sci U S A *117*, 3114-3122.
653 Li, D., Edwards, R.J., Manne, K., Martinez, D.R., Schafer, A., Alam, S.M., Wiehe, K., Lu, X., Parks,
654 R., Sutherland, L.L., *et al.* (2021). The functions of SARS-CoV-2 neutralizing and infection-
655 enhancing antibodies in vitro and in mice and nonhuman primates. bioRxiv.
656 Liu, L., Wang, P., Nair, M.S., Yu, J., Rapp, M., Wang, Q., Luo, Y., Chan, J.F., Sahi, V., Figueroa, A.,
657 *et al.* (2020). Potent neutralizing antibodies against multiple epitopes on SARS-CoV-2 spike.
658 Nature *584*, 450-456.
659 Lowy, D.R., and Schiller, J.T. (2006). Prophylactic human papillomavirus vaccines. J Clin
660 Invest *116*, 1167-1173.
661 Marcandalli, J., Fiala, B., Ols, S., Perotti, M., de van der Schueren, W., Snijder, J., Hodge, E.,
662 Benhaim, M., Ravichandran, R., Carter, L., *et al.* (2019). Induction of Potent Neutralizing
663 Antibody Responses by a Designed Protein Nanoparticle Vaccine for Respiratory Syncytial
664 Virus. Cell *176*, 1420-1431 e1417.

16

665 Menachery, V.D., Yount, B.L., Jr., Debbink, K., Agnihothram, S., Gralinski, L.E., Plante, J.A.,
666 Graham, R.L., Scobey, T., Ge, X.Y., Donaldson, E.F., *et al.* (2015). A SARS-like cluster of
667 circulating bat coronaviruses shows potential for human emergence. Nat Med *21*, 1508-
668 1513.
669 Modjarrad, K., Roberts, C.C., Mills, K.T., Castellano, A.R., Paolino, K., Muthumani, K.,
670 Reuschel, E.L., Robb, M.L., Racine, T., Oh, M.D., *et al.* (2019). Safety and immunogenicity of
671 an anti-Middle East respiratory syndrome coronavirus DNA vaccine: a phase 1, open-label,
672 single-arm, dose-escalation trial. Lancet Infect Dis *19*, 1013-1022.
673 Moyo-Gwete, T., Madzivhandila, M., Makhado, Z., Ayres, F., Mhlanga, D., Oosthuysen, B.,
674 Lambson, B.E., Kgagudi, P., Tegally, H., Iranzadeh, A., *et al.* (2021). SARS-CoV-2 501Y.V2
675 (B.1.351) elicits cross-reactive neutralizing antibodies. bioRxiv.
676 Om, K., Paquin-Proulx, D., Montero, M., Peachman, K., Shen, X., Wieczorek, L., Beck, Z.,
677 Weiner, J.A., Kim, D., Li, Y., *et al.* (2020). Adjuvanted HIV-1 vaccine promotes antibody-
678 dependent phagocytic responses and protects against heterologous SHIV challenge. PLoS
679 Pathog *16*, e1008764.
680 Pallesen, J., Wang, N., Corbett, K.S., Wrapp, D., Kirchdoerfer, R.N., Turner, H.L., Cottrell, C.A.,
681 Becker, M.M., Wang, L., Shi, W., *et al.* (2017). Immunogenicity and structures of a rationally
682 designed prefusion MERS-CoV spike antigen. Proc Natl Acad Sci U S A *114*, E7348-E7357.
683 Pati, R., Shevtsov, M., and Sonawane, A. (2018). Nanoparticle Vaccines Against Infectious
684 Diseases. Front Immunol *9*, 2224.
685 Piehler, B., Nelson, E.K., Eckels, J., Ramsay, S., Lum, K., Wood, B., Greene, K.M., Gao, H.,
686 Seaman, M.S., Montefiori, D.C., *et al.* (2011). LabKey Server NAb: a tool for analyzing,
687 visualizing and sharing results from neutralizing antibody assays. BMC Immunol *12*, 33.
688 Pinto, D., Park, Y.J., Beltramello, M., Walls, A.C., Tortorici, M.A., Bianchi, S., Jaconi, S., Culap,
689 K., Zatta, F., De Marco, A., *et al.* (2020). Cross-neutralization of SARS-CoV-2 by a human
690 monoclonal SARS-CoV antibody. Nature *583*, 290-295.
691 Plotkin, S.A. (2017). Vaccines for epidemic infections and the role of CEPI. Hum Vaccin
692 Immunother *13*, 2755-2762.
693 Powell, A.E., Zhang, K., Sanyal, M., Tang, S., Weidenbacher, P.A., Li, S., Pham, T.D., Pak, J.E.,
694 Chiu, W., and Kim, P.S. (2021). A Single Immunization with Spike-Functionalized Ferritin
695 Vaccines Elicits Neutralizing Antibody Responses against SARS-CoV-2 in Mice. ACS Cent Sci
696 *7*, 183-199.
697 Rappazzo, C.G., Tse, L.V., Kaku, C.I., Wrapp, D., Sakharkar, M., Huang, D., Deveau, L.M.,
698 Yockachonis, T.J., Herbert, A.S., Battles, M.B., *et al.* (2021). Broad and potent activity against
699 SARS-like viruses by an engineered human monoclonal antibody. Science *371*, 823-829.
700 Salazar, E., Christensen, P.A., Graviss, E.A., Nguyen, D.T., Castillo, B., Chen, J., Lopez, B.V.,
701 Eagar, T.N., Yi, X., Zhao, P., *et al.* (2020). Treatment of Coronavirus Disease 2019 Patients
702 with Convalescent Plasma Reveals a Signal of Significantly Decreased Mortality. Am J Pathol
703 *190*, 2290-2303.
704 Sauer, M.M., Tortorici, M.A., Park, Y.-J., Walls, A.C., Homad, L., Acton, O., Bowen, J., Wang, C.,
705 Xiong, X., de van der Schueren, W., *et al.* (2021). Structural basis for broad coronavirus
706 neutralization. bioRxiv, 2020.2012.2029.424482.
707 Saunders, K.O., Lee, E., Parks, R., Martinez, D.R., Li, D., Chen, H., Edwards, R.J., Gobeil, S., Barr,
708 M., Mansouri, K., *et al.* (2021). SARS-CoV-2 vaccination induces neutralizing antibodies
709 against pandemic and pre-emergent SARS-related coronaviruses in monkeys. bioRxiv,
710 2021.2002.2017.431492.

17

711   Shen, C., Wang, Z., Zhao, F., Yang, Y., Li, J., Yuan, J., Wang, F., Li, D., Yang, M., Xing, L., *et al.*
712   (2020). Treatment of 5 Critically Ill Patients With COVID-19 With Convalescent Plasma.
713   JAMA *323*, 1582-1589.
714   ter Meulen, J., van den Brink, E.N., Poon, L.L., Marissen, W.E., Leung, C.S., Cox, F., Cheung,
715   C.Y., Bakker, A.Q., Bogaards, J.A., van Deventer, E., *et al.* (2006). Human monoclonal
716   antibody combination against SARS coronavirus: synergy and coverage of escape mutants.
717   PLoS Med *3*, e237.
718   Tian, X., Li, C., Huang, A., Xia, S., Lu, S., Shi, Z., Lu, L., Jiang, S., Yang, Z., Wu, Y., *et al.* (2020).
719   Potent binding of 2019 novel coronavirus spike protein by a SARS coronavirus-specific
720   human monoclonal antibody. Emerg Microbes Infect *9*, 382-385.
721   Turonova, B., Sikora, M., Schurmann, C., Hagen, W.J.H., Welsch, S., Blanc, F.E.C., von Bulow,
722   S., Gecht, M., Bagola, K., Horner, C., *et al.* (2020). In situ structural analysis of SARS-CoV-2
723   spike reveals flexibility mediated by three hinges. Science *370*, 203-208.
724   Ueda, G., Antanasijevic, A., Fallas, J.A., Sheffler, W., Copps, J., Ellis, D., Hutchinson, G.B.,
725   Moyer, A., Yasmeen, A., Tsybovsky, Y., *et al.* (2020). Tailored design of protein nanoparticle
726   scaffolds for multivalent presentation of viral glycoprotein antigens. Elife *9*.
727   Walls, A.C., Fiala, B., Schafer, A., Wrenn, S., Pham, M.N., Murphy, M., Tse, L.V., Shehata, L.,
728   O'Connor, M.A., Chen, C., *et al.* (2020). Elicitation of Potent Neutralizing Antibody
729   Responses by Designed Protein Nanoparticle Vaccines for SARS-CoV-2. Cell *183*, 1367-1382
730   e1317.
731   Walls, A.C., Tortorici, M.A., Bosch, B.J., Frenz, B., Rottier, P.J.M., DiMaio, F., Rey, F.A., and
732   Veesler, D. (2016). Cryo-electron microscopy structure of a coronavirus spike glycoprotein
733   trimer. Nature *531*, 114-117.
734   Wang, L., Shi, W., Joyce, M.G., Modjarrad, K., Zhang, Y., Leung, K., Lees, C.R., Zhou, T., Yassine,
735   H.M., Kanekiyo, M., *et al.* (2015). Evaluation of candidate vaccine approaches for MERS-CoV.
736   Nat Commun *6*, 7712.
737   Wang, L., Zhou, T., Zhang, Y., Yang, E.S., Schramm, C.A., Shi, W., Pegu, A., Oloninyi, O.K.,
738   Ransier, A., Darko, S., *et al.* (2021). Antibodies with potent and broad neutralizing activity
739   against antigenically diverse and highly transmissible SARS-CoV-2 variants. bioRxiv.
740   Wibmer, C.K., Ayres, F., Hermanus, T., Madzivhandila, M., Kgagudi, P., Oosthuysen, B.,
741   Lambson, B.E., de Oliveira, T., Vermeulen, M., van der Berg, K., *et al.* (2021). SARS-CoV-2
742   501Y.V2 escapes neutralization by South African COVID-19 donor plasma. Nat Med.
743   Wrapp, D., De Vlieger, D., Corbett, K.S., Torres, G.M., Wang, N., Van Breedam, W., Roose, K.,
744   van Schie, L., Team, V.-C.C.-R., Hoffmann, M., *et al.* (2020). Structural Basis for Potent
745   Neutralization of Betacoronaviruses by Single-Domain Camelid Antibodies. Cell *181*, 1004-
746   1015 e1015.
747   Zheng, J., Wong, L.R., Li, K., Verma, A.K., Ortiz, M.E., Wohlford-Lenane, C., Leidinger, M.R.,
748   Knudson, C.M., Meyerholz, D.K., McCray, P.B., Jr., *et al.* (2021). COVID-19 treatments and
749   pathogenesis including anosmia in K18-hACE2 mice. Nature *589*, 603-607.
750   Zost, S.J., Gilchuk, P., Case, J.B., Binshtein, E., Chen, R.E., Nkolola, J.P., Schafer, A., Reidy, J.X.,
751   Trivette, A., Nargi, R.S., *et al.* (2020). Potently neutralizing and protective human antibodies
752   against SARS-CoV-2. Nature *584*, 443-449.
753
754
755   **STAR METHODS**

756 Detailed methods are provided in the online version of this paper and include the
757 following:
758
759 KEY RESOURCES TABLE
760 RESOURCE AVAILABILITY
761   Lead contact
762   Materials availability
763   Data and code availability statement
764 METHOD DETAILS
765   Immunogen Modeling and Design
766   DNA plasmid construction and preparation
767   Protein expression and purification
768   Negative-stain Electron microscopy
769   Octet Biolayer Interferometry binding and ACE2 inhibition assays
770   Mouse immunization
771   Immunogen-Adjuvant preparations
772   Enzyme Linked Immunosorbent Assay
773   SARS-CoV-2 and SARS-CoV-1 pseudovirus neutralization assay
774   Authentic SARS-CoV-2 virus neutralization assay
775   K18-hACE2 transgenic mouse passive immunization and challenge
776
777 QUANTIFICATION AND STATISTICAL ANALYSIS
778
779 **RESOURCE AVAILABILITY**
780
781 **Lead contact**
782 Further information and requests for resources and reagents should be directed to and will
783 be fulfilled by the Lead Contact, M. Gordon Joyce (gjoyce@eidresearch.org).
784
785 **Materials Availability**
786 All reagents will be made available on request after completion of a Materials Transfer
787 Agreement.
788
789 **Data and Code Availability**
790 All data supporting the findings of this study are found within the paper and its
791 Supplementary Information and are available from the Lead Contact author upon request.
792
793 **Figure legends**
794 **Figure 1. Structure-based design of SARS-CoV-2 S-based ferritin nanoparticle**
795 **immunogens**
796 (A) Full length SARS-CoV-2 S schematic and 3D-structure. S hinges identified by molecular
797 dynamics simulations and electron cryotomography are labeled on the 3D- model
798 ((Turonova et al., 2020). The structured trimeric ectodomain is colored according to the
799 schematic with the N-terminal domain (NTD) and Receptor-Binding Domain (RBD) of the
800 S1 polypeptide and the C-terminal coiled coil N-terminal to hinge 1 colored blue, green, and
801 purple, respectively. Remaining portions of the S1 and S2 polypeptides are colored in red

19

802 and cyan with regions membrane-proximal from hinge 2 colored in white. The
803 transmembrane domain of all chains is depicted in yellow. To design a Spike-Ferritin
804 molecule, the C-terminal heptad repeat (residues 1140 to 1161) between Hinge 1 and 2
805 were aligned to an ideal heptad repeat sequence. Residues in the native S sequence which
806 break this pattern are highlighted in red. These residues are also labeled and highlighted in
807 red on the 3D-structure. Two engineered designs (1B-05 and 1B-06) are shown, with S end
808 residue used to link to Ferritin, and heptad-repeat mutations colored green.
809 (B) Schematic and 3D model of Spike Ferritin nanoparticle (SpFN). Differences between the
810 native S sequence and the engineered nanoparticle are indicated on the schematic. A 3D-
811 model of SpFN displaying eight trimeric Spikes was created using PDB ID 6VXX and 3EGM
812 with the ferritin molecule shown in alternating grey and white. The nanoparticle is
813 depicted along the 4-fold and the 3-fold symmetry axes of the ferritin.
814 (C) RBD–Ferritin nanoparticle design and optimization. The RBD of SARS-CoV-2 (PDB
815 ID:6MOJ) is shown in surface representation, with the ACE2 binding site outlined in dashed
816 lines. Three hydrophobic regions of the RBD which were mutated for nanoparticle
817 immunogen design are shown in light green surface, with residues in stick representation.
818 The ACE2 binding site contains two of these regions, while a third hydrophobic patch near
819 the C-terminus of the RBD is typically buried by S2 and part of S1 in the context of the
820 trimer molecule.
821 (D) Schematic and 3D model of an RBD–Ferritin nanoparticle. A modeled 24-mer
822 nanoparticle displaying the RBD domain is depicted at the 3-fold symmetry axis of ferritin
823 and colored green. Truncation points, linkers, and alterations made to the RBD sequence
824 are indicated on the schematic.
825 (E) Schematic and 3D model of an RBD–NTD–Ferritin nanoparticle. A modeled nanoparticle
826 displaying RBD and NTD epitopes is depicted and colored according to the schematic.
827 Truncation points, linkers, and alterations made to the native S sequence are indicated on
828 the primary structure.
829 (F) S1-Ferritin immunogen design. The SARS-CoV-2 S1 forms a hydrophobic collar around
830 the N-terminal β-sheet of S2 (residues 689-676). S1-ferritin immunogen design required
831 inclusion of this short stretch of S2 (colored cyan) attached by a linker. Terminal residues
832 of the structured portions of S1 and S2 are labeled.
833 (G) Schematic and 3D model of an S1–Ferritin nanoparticle. A modeled nanoparticle
834 displaying RBD and NTD domains is depicted and colored according to the S1–ferritin
835 schematic with truncation points and domain linkers indicated. See also Figure S1 and
836 Table S1.
837
838 **Figure 2. Antigenic and biophysical characterization of SARS-CoV-2 Spike-based**
839 **ferritin nanoparticle vaccine candidates**
840 SDS-PAGE of (A) Spike-Ferritin nanoparticle designs, (B) Receptor-binding domain-Ferritin
841 nanoparticle designs, (C) S1-ferritin nanoparticle, and (D) RBD-NTD-Ferritin nanoparticles.
842 Molecular weight standards are indicated in kDa.
843 (E) Size-exclusion chromatography on a Superdex S200 10/300 column of representative
844 SARS-CoV-2 S-based ferritin nanoparticles. (F) Negative-stain electron microscopy 2D class
845 averages of purified nanoparticles. The black bars represent 50 nm. See also Figure S2 and
846 S3.
847

848 **Figure 3. Antigenic characterization of select SARS-CoV-2 Spike-based ferritin**
849 **nanoparticle vaccine candidates**
850 Binding response of SARS-CoV-2 neutralizing antibodies to each of the lead candidates
851 from the four design categories measured by biolayer interferometry with two-fold serial
852 dilution of each antibody starting at 30 μg/ml).
853 (A) Spike-Ferritin nanoparticle SpFN_1B-06-PL.
854 (B) RBD-Ferritin pCoV131.
855 (C) RBD-NTD-Ferritin nanoparticle pCoV146.
856 (D) S1-Ferritin nanoparticle pCoV111.
857 See also Figure S3.
858
859 **Figure 4. Negative-Stain Electron Microscopy 3D Reconstructions of SARS-CoV-2**
860 **Spike Domain-Ferritin Nanoparticles**
861 Modifications made to native sequence and linkers used for each construct are shown in
862 schematic diagrams.
863 (A) Negative-stain 3D reconstructions with applied octahedral symmetry are shown with
864 an asymmetric unit of non-ferritin density colored and the size of each particle indicated in
865 nanometers. Spike trimer density, is colored in red, and a model of a SpFN trimer based on
866 PDB 6VXX is shown docked into the negative-stain map and colored according to the
867 sequence diagram.
868 (B) Two non-ferritin densities per asymmetric unit were observed for RFN and are
869 highlighted in green. These densities putatively correspond to the receptor-binding domain
870 (RBD) but lack low resolution distinguishing features due to the small, globular shape of
871 these domains. The presence of two densities is likely due to flexibility in the linker and
872 heterogeneity in the RBD pose.
873 (C) Two layers of densities were distinguishable for pCoV146, with the putative N-terminal
874 domain (NTD) density of an asymmetric unit colored blue, proximal to the ferritin and two
875 smaller, more flexible densities corresponding to RBD distal to the ferritin and colored
876 green.
877 (D) An asymmetric unit of non-ferritin density for pCoV111 is colored in orange and a
878 monomer of S1 in the closed trimer state from PDB 6VXX is shown docked into the density
879 with domains colored as in the sequence diagram.
880 See also Figure S2 and Table S2.
881
882 **Figure 5 SARS-CoV-2 Spike-domain nanoparticle vaccine candidates elicit robust**
883 **binding and neutralizing antibody responses in mice.**
884 (A) Biolayer interferometry binding of mouse sera to SARS-COV-2 RBD. Study week is
885 indicated on the base of the graph. Mean value is indicated by a horizontal line. Statistical
886 comparison at each timepoint was carried out using a a Kruskal-Wallis test followed by a
887 Dunn's post-test.
888 (B) ELISA binding of mouse sera to SARS-COV-2 S-2P or RBD. Study week is indicated on
889 the base of the graph. Geometric mean value is indicated by a horizontal line. Statistical
890 comparison at each timepoint was carried out using a a Kruskal-Wallis test followed by a
891 Dunn's post-test.

21

892   (C) SARS-COV-2 pseudovirus neutralization ID50 and ID80 values. Geometric mean value is
893   indicated by a horizontal line. Statistical comparisons at each given timepoint was carried
894   out using a Kruskal-Wallis test followed by a Dunn's post-test.
895   (D) Binding and pseudovirus neutralization of sera from mice immunized with 0.08 µg
896   SpFN + ALFQ.
897   (E) Authentic SARS-CoV-2 virus strain 2019-nCoV/USA_WA1/2020 neutralization ID50
898   and ID80 are shown for mice immunized with 10 or 0.08 µg SpFN + ALFQ. Geometric mean
899   value is indicated by a horizontal line. Comparisons between dose group at each time point
900   were carried out using a Mann-Whitney unpaired two-tailed non-parametric test, n=10
901   mice/group.
902   In panels A – C, all immunogen groups at a given study timepoint were compared to each
903   other. Only groups with statistically significant differences are indicated by a bar; all other
904   groups did not show statistically significant differences. P values <0.0001 (****), <0.001
905   (***), <0.01 (**), or <0.05 (*).
906   See also Figure S4 and S5, and Table S3 and S4.
907
908   **Figure 6. SpFN- and RBD-FN protective immunity in K18-hACE2 transgenic mice.**
909   (A) IgG was purified from SPFN- or RFN-vaccinated mouse sera and passively transferred
910   at specific IgG amounts ranging from 4 - 470 µg/mouse in a final volume of 200 µl. Control
911   naïve mouse IgG was formulated at 2 mg/ml. (n=10/group, 5 female, 5 male).
912   (B) Mouse challenge study schematic. K18-hACE2 mice (n=10/group, 5 female, 5 male)
913   received control IgG (black), PBS (gray), and purified IgG, one day prior to challenge with
914   1.25×10^4 PFU of SARS-CoV-2.
915   (C) SARS-CoV-2 pseudovirus neutralization ID_{50} titers of mouse sera at study day 0.
916   (D) Percentage of initial weight of K18-hACE2 mice for the 8 study groups. Legend is shown
917   in panel E.
918   (E) Survival curves of K18-hACE2 mice with groups indicated based on animal vaccination
919   group and the pseudovirus ID_{50} neutralization values. Statistical comparisons were carried
920   out using Mantel-Cox test followed by Bonferroni correction.
921   See also Figure S6.
922
923   **Figure 7. SARS-CoV-2 Spike-domain nanoparticle vaccine candidates elicit robust**
924   **antibody binding responses and neutralizing activity against SARS-CoV-2 VoC and**
925   **SARS-CoV-1.**
926   (A) Biolayer Interferometry binding of study week 10 immunized C57BL/6 mouse serum
927   to SARS-CoV-2 RBD, and SARS-CoV-2 RBD variants. Immunogens are indicated at the top
928   left of each graph. Mean values are indicated by a horizontal line, n=10, Significance was
929   assessed using a Kruskal-Wallis test followed by a Dunn's post-test.
930   (B) Pseudovirus neutralization (ID_{50} values) of study week 10 immunized C57BL/6 and
931   BALB/c mouse serum to SARS-CoV-2 Wuhan-1, B.1.1.7, and B.1.351 pseudotyped viruses.
932   Immunogens are indicated at the base of each graph. Geometric mean values are indicated
933   by a horizontal line, n=5, statistical significance for each immunogen was assessed using a
934   Kruskal-Wallis test followed by a Dunn's post-test.
935   (C) Biolayer Interferometry binding of study week 10 immunized C57BL/6 and BALB/c
936   mouse serum to SARS-CoV-1 RBD. Immunogens are indicated at the base of each graph.

937   Mean values are indicated by a horizontal line, n=10, Significance was assessed using a
938   Kruskal-Wallis test followed by a Dunn's post-test.
939   (D) Pseudovirus neutralization (ID$_{50}$ values) of study week 10 immunized C57BL/6 and
940   BALB/c mouse serum to SARS-CoV-1 Urbani strain pseudotyped viruses. Data related to
941   SpFN and RFN are colored blue and green respectively. Statistical comparisons between
942   SpFN and RFN responses at each time point were carried out using a Mann-Whitney
943   unpaired two-tailed non-parametric test.
944   Immunogens are indicated at the base of each graph. Geometric mean values are indicated
945   by a horizontal line, n=10, P values <0.0001 (****), <0.01 (**) or <0.05 (*).
946   See also Figure S4 and S5.
947
948   **List of supplementary figures.**
949   **Figure S1. Structure-based design of SARS-CoV-2 Spike-based ferritin nanoparticle**
950   **immunogens and design pipeline, related to Figure 1.**
951   Four ferritin nanoparticle immunogen designs were developed focused on (1) Spike
952   ferritin nanoparticles (blue), (2) RBD ferritin nanoparticles (green), (3) RBD-NTD ferritin
953   nanoparticles (black), and (4) S1 ferritin nanoparticles (orange). The design iterations and
954   concepts are indicated, along with select mutations and design name. Lead vaccine
955   candidates from each category are highlighted.
956
957   **Figure S2. Negative-stain electron microscopy 2D micrographs of SARS-CoV-2 ferritin**
958   **nanoparticle-based vaccine candidates, related to Figure 2 and 4.**
959   Negative-stain electron microscopy 2D micrographs. The white scale bars represent 100
960   nm.
961   (A) Spike ferritin nanoparticles pCoV1B-05 and pCoV1B-08.
962   (B) RBD ferritin nanoparticles pCoV03, pCoV50, pCOV58, pCoV59, pCoV127, pCoV129,
963   pCoV130, pCoV131
964   (C) RBD-NTD ferritin nanoparticles pCoV122, pCoV125, pCoV147
965   (D) S1 ferritin nanoparticle pCoV110 and pCoV112.
966
967   **Figure S3. Biophysical and antigenic characterization of S-domain ferritin**
968   **nanoparticle immunogens, related to Figure 2 and 3.**
969   (A) Size-exclusion chromatography on a Superdex S200 10/300 column of representative
970   SARS-CoV-2 Spike-based ferritin nanoparticles from the four design categories.
971   (B) Expression levels (mg/L supernatant) of representative SARS-CoV-2 Spike-based
972   ferritin nanoparticles.
973   (C) Dynamic light scattering analysis of representative SARS-CoV-2 Spike-based ferritin
974   nanoparticles.
975   (D) Spike ferritin nanoparticles (E) RBD ferritin, (F) RBD-NTD ferritin and (G) S1 ferritin
976   nanoparticles were assessed for binding to a set of neutralizing antibodies (concentration =
977   30 µg/ml) by biolayer interferometry.
978
979   **Figure S4 SARS-CoV-2 nanoparticle vaccine candidates elicit robust binding and**
980   **pseudovirus neutralizing antibody responses in mice. Related to Figure 5 and 7.**

981 (A) Biolayer Interferometry binding analysis of C57BL/6 and BALB/c sera from mice
982 immunized with SpFN + Alhydrogel® (B) RFN + Alhydrogel® and (C) pCoV146 +
983 Alhydrogel® to SARS-CoV-2 RBD. Mean values are indicated by a horizontal line, n=10.
984 (D) Pseudovirus neutralization (ID_{50} values) of C57BL/6 and BALB/c sera from mice
985 immunized with SpFN + Alhydrogel® (E) RFN + Alhydrogel® and (F) pCoV146 +
986 Alhydrogel®. Geometric mean values are indicated by a horizontal line, n=10.
987 (G) ELISA analysis of antibody isotype usage following immunization with SpFN + ALFQ
988 (solid shapes), or SpFN + Alhydrogel® (open shapes). Sera collected study week 2, 5, and 8
989 from immunized mice were added in quadruplicate serial dilutions to ELISA plates coated
990 with S-2P protein. Duplicated wells were probed with anti-mouse-IgG1-HRP. Additional
991 duplicates were probed with either anti-mouse-IgG2c-HRP or anti-mouse IgG2a-HRP for
992 C57BL/6 and BALB/c mice, respectively. Data was interpolated to obtain the dilution factor
993 at OD_{450} of 1 and plotted as ratios of IgG2/IgG1. A horizontal dotted line denotes a
994 balanced 1:1 IgG2/IgG1 ratio. Isotype ratio values were compared between the two
995 adjuvant groups at each timepoint for each mouse type using a Mann-Whitney unpaired
996 two-tailed non-parametric test.
997 (H) Biolayer interferometry analysis of BALB/c mouse sera binding to SARS-CoV-2 RBD at
998 study weeks 2, 5 and 8. Mice were immunized with the four lead candidate vaccines SpFN
999 (blue), RFN (green), pCoV146 (black) and pCOV111 (orange). Binding mean values are
1000 indicated by a horizontal line, n=10, sera responses at a given study week were compared
1001 for statistical differences using a Kruskal-Wallis test followed by a Dunn's post-test.
1002 (I) ELISA analysis of BALB/c mice immune responses as indicated in (H). Binding
1003 geometric mean values of the endpoint titers are indicated by a horizontal line, n=10, sera
1004 responses at a given study week were compared for statistical differences using a Kruskal-
1005 Wallis test followed by a Dunn's post-test.
1006 (J) Pseudovirus neutralization ID50 titers of BALB/c mice immunized as indicated in (H).
1007 Geometric mean values are indicated by a horizontal line, n=10, sera neutralization titers at
1008 a given study week for the four immunogens were compared for statistical differences
1009 using a Kruskal-Wallis test followed by a Dunn's post-test.
1010 (K) Pseudovirus neutralization ID_{80} titers of C57BL/6 (left) and BALB/c mice (right)
1011 immunized as indicated in (H). Geometric mean values are indicated by a horizontal line,
1012 n=10, sera neutralization titers at a given study week for the four immunogens were
1013 compared for statistical differences using a Kruskal-Wallis test followed by a Dunn's post-
1014 test.
1015 P values <0.0001 (****), <0.001 (***), <0.01 (**) or <0.05 (*).
1016
1017 **Figure S5 SARS-CoV-2 SpFN vaccine candidate elicits robust binding and neutralizing**
1018 **antibody responses at reduced doses in mice. Related to Figure 5 and 7.**
1019 (A) Biolayer interferometry analysis of C57BL/6 and (B) BALB/c mouse sera binding
1020 response to SARS-CoV-2 RBD following immunization with reducing doses of SpFN.
1021 (C, E) ELISA analysis of C57BL/6 and (D, F) BALB/c mouse sera binding response to SARS-
1022 CoV-2 RBD or S-2P following immunization with reducing doses of SpFN.
1023 (G) SARS-CoV-2 pseudovirus ID80 neutralization titers of mice immunized with 0.08 µg
1024 SpFN + ALFQ.
1025 (H) Authentic SARS-CoV-2 virus ID80 neutralization titers of mice immunized with 10 µg
1026 (blue) or 0.08 µg (light blue) SpFN + ALFQ. Geometric mean titers for each group and time

1027   point are indicated by a horizontal line, n =10. Neutralization titers for the two dose
1028   groups at each study time point were compared for statistically significant differences
1029   using a Mann-Whitney unpaired two-tailed non-parametric test. The two BALB/c time
1030   points that showed differences are indicated by bars. P values <0.001 (***), <0.01 (**).
1031   (I) Mouse sera from study week 10 was analyzed for hACE2 blocking capacity to SARS-CoV-
1032   2 RBD (left) or SARS-CoV-1 RBD using a biolayer interferometry assay format.
1033
1034   **Figure S6 Histopathological analysis of SARS-CoV-2 infection in K18-ACE2 mice.**
1035   **Related to Figure 7**
1036   (A, B) Hematoxylin and eosin staining of lung sections from K18-hACE2 mice following
1037   intranasal infection with 1.25×10^4 PFU SARS-CoV-2. Images show two magnifications.
1038   Images are representative of n = 10 per group.
1039
1040

1041 **Table S1. Spike-domain ferritin immunogens**

1042

Construct ID	Description		Leader
Spike-Ferritin (all based on S-2P variant with Δfurin and PP)			
pCoV1B-01	S2P(1-1137)-del-4-Ferritin	Shortened ectodomain - no coiled coil (closest to flu HA pass off)	NL
pCoV1B-02	S2P(1-1137)-del-6-Ferritin	Shortened ectodomain - no coiled coil (closest to flu HA pass off)	NL
pCoV1B-03	S2P(1-1208)-del-Ferritin	Full ectodomain	NL
pCoV1B-04	S2P(1-1208)-GCN4-Ferritin	Full ectodomain with GCN4	NL
pCoV1B-05	S2P(1-1154)-del-Ferritin	Shortened ectodomain with ending with a couple turns of coiled coil	NL
pCoV1B-06	S2P(1-1158)op1-del-Ferritin	Optimized HR ending (end on glycan N1158)	NL
pCoV1B-07	S2P(1-1158)op2-del-Ferritin	Optimized HR ending (Ile) (end on glycan N1158)	NL
pCoV1B-08	S2P(1-1158)op1x2-del-Ferritin	Optimized HR ending (N1158 glycan removed, but exists on the repeated HR)	NL
pCoV1B-09	S2P(1-1158)op2x2-del-Ferritin	Optimized HR ending (Ile) (N1158 glycan removed, but exists on the repeated HR)	NL
pCoV1B-10	S2P(1-1158)op1-fGCN4-del-Ferritin	Optimized HR ending with GCN4 fused in register (no glycan N1158)	NL
pCoV1B-01-PL	PL-S2P(12-1137)-del-4-Ferritin	Shortened ectodomain - no coiled coil (closest to flu HA pass off)	PL
pCoV1B-02-PL	PL-S2P(12-1137)-del-6-Ferritin	Shortened ectodomain - no coiled coil (closest to flu HA pass off)	PL
pCoV1B-03-PL	PL-S2P(12-1208)-del-Ferritin	Full ectodomain	PL
pCoV1B-04-PL	PL-S2P(12-1208)-GCN4-Ferritin	Full ectodomain with GCN4	PL
pCoV1B-05-PL	PL-S2P(12-1154)-del-Ferritin	Shortened ectodomain with ending with a couple turns of coiled coil	PL
pCoV-1B-06-PL (aka SpFN)	PL-S2P(12-1158)op1-del-Ferritin	Optimized HR ending (end on glycan N1158)	PL
pCoV1B-07-PL	PL-S2P(12-1158)op2-del-Ferritin	Optimized HR ending (Ile) (end on glycan N1158)	PL
pCoV1B-08-PL	PL-S2P(12-1158)op1x2-del-Ferritin	Optimized HR ending (N1158 glycan removed, but exists on the repeated HR)	PL
pCoV1B-09-PL	PL-S2P(12-1158)op2x2-del-Ferritin	Optimized HR ending (Ile) (N1158 glycan removed, but exists on the repeated HR)	PL
pCoV1B-10-PL	PL-S2P(12-1158)op1-fGCN4-del-Ferritin	Optimized HR ending with GCN4 fused in register (no glycan N1158)	PL

Construct ID	Description	Comment	Leader
RBD-Ferritin			
pCoV03	His8-3C-RBD(331-527)-Ferritin	N-terminal His8 with HRV-3C cleavage site, GSGGGG linker between RBD and Ferritin	PL
pCoV29	His8-3C-RBD-3-Ferritin	SGG linker	PL
pCoV30	His8-3C-RBD-3-del-Ferritin	SGG linker, Δ first 10 residues in ferritin, then DIEK changed to DIIK	PL
pCoV31	His8-3C-RBD-6-del-Ferritin	P527G, Δ first 8 residues in ferritin, then SKDIEK changed to DIIK	PL
pCoV1A-01	His8-3C-RBD-PPII-Ferritin	Extend distance between RBD and ferritin - using polyproline Helix	PL
pCoV1A-02	His8-3C-RBD-alpha1-Ferritin	Extend distance between RBD and ferritin - using alpha Helix from bottom of S protein	PL
pCoV1A-03	His8-3C-RBD-alpha2-Ferritin	Extend distance between RBD and ferritin- using alpha Helix from bottom of S protein	PL
pCoV1A-04	His8-3C-RBD-GCN4-del-Ferritin	Extend distance between RBD and ferritin + stabilize ferritin - using GCN4 trimerization motif	PL

26

Construct ID	Description		
pCoV1A-05	His8-3C-RBD-1141_1158op1-del-Ferritin	Extend distance between RBD and ferritin + stabilize ferritin - using semi-native trimerization motif	PL
pCoV1A-06	His8-3C-RBD-1141_1158op1x2-del-Ferritin	Extend distance between RBD and ferritin + stabilize ferritin - using semi-native trimerization motif	PL
pCoV49	His8-3C-RBD-F456N/K458T-Ferritin	RBD with indicated point mutations	PL
pCoV50	His8-3C-RBD-L455R/Y449K/F490R-Ferritin	RBD with indicated point mutations	PL
pCoV51	His8-3C-RBD-L455R-Ferritin	RBD with indicated point mutation	PL
pCoV52	His8-3C-RBD-I468R-Ferritin	RBD with indicated point mutation	PL
pCoV53	His8-3C-RBD-Y453R-Ferritin	RBD with indicated point mutation	PL
pCoV54	His8-3C-RBD-L452R-Ferritin	RBD with indicated point mutation	PL
pCoV55	His8-3C-RBD-L492R-Ferritin	RBD with indicated point mutation	PL
pCoV56	His8-3C-RBD-F490R-Ferritin	RBD with indicated point mutation	PL
pCoV57	His8-3C-RBD-F490A-Ferritin	RBD with indicated point mutation	PL
pCoV58	His8-3C-RBD-L518N/L519K/H520S-Ferritin	RBD with indicated point mutations	PL
pCoV59	His8-3C-RBD-L518R-Ferritin	RBD with indicated point mutation	PL
pCoV60	His8-3C-RBD-V367T/L335N-Ferritin	RBD with indicated point mutations	PL
pCoV61	His8-3C-RBD-T385N/L387T-Ferritin	RBD with indicated point mutations	PL
pCoV62	His8-3C-RBD-V382R-Ferritin	RBD with indicated point mutation	PL
pCoV63	His8-3C-RBD-F377R-Ferritin	RBD with indicated point mutation	PL
pCoV127	His8-3C-RBD-F490A/L518N/L519K/H520S-Ferritin	RBD with indicated point mutations	PL
pCoV128	His8-3C-RBD-F490A/L518R-Ferritin	RBD with indicated point mutations	PL
pCoV129	His8-3C-RBD-L455R/Y449K/F490R/L518N/L519K/H520S-Ferritin	RBD with indicated point mutations	PL
pCoV130	His8-3C-RBD-L455R/Y449K/F490R/L518R-Ferritin	RBD with indicated point mutations	PL
pCoV131 (aka RFN)	His8-3C-RBD-Y453R/L518N/L519K/H520S-Ferritin	RBD with indicated point mutations	PL
pCoV132	His8-3C-RBD-Y453R/L518R-Ferritin	RBD with indicated point mutations	PL

RBD-NTD-Ferritin			
Construct ID	Description		
pCoV122	His8-3C-RBD(331-527)-GSGGSG-NTD(12-303)-Ferritin	N-terminal HIs8 with HRV-3C cleavage site, GSGGSG linker between RBD and NTD, GSGGGG linker between NTD and Ferritin	PL
pCoV123	His8-3C-RBD-F490R-NTD-Ferritin	RBD with indicated point mutation	PL
pCoV124	His8-3C-RBD-F490A-NTD-Ferritin	RBD with indicated point mutation	PL
pCoV125	His8-3C-RBD-L518N/L519K/H520S-NTD-Ferritin	RBD with indicated point mutations	PL
pCoV126	His8-3C-RBD-L518R-NTD-Ferritin	RBD with indicated point mutation	PL
pCoV146	His8-3C-RBD-Y453R-L518N/L519K/H520S-NTD-Ferrritin	RBD with indicated point mutations	PL
pCoV147	His8-3C-RBD-F490A-L518N/L519K/H520S-NTD-Ferrritin	RBD with indicated point mutations	PL

S1-Ferritin			
Construct ID	Description		
pCoV68	S1(12-678)-Ferritin	GSGGSG linker between S1 and Ferritin	PL
pCoV107	S1(12-655)-Ferritin	24 residues removed from the C-terminus	PL
pCoV108	S1(12-655)-L611N/Q613T-Ferritin	24 residues removed from the C-terminus, S1 with indicated point mutations	PL
pCoV109	S1(12-696)-Ferritin	Extended the sequence to include a portion of S2	PL
pCoV110	S1(12-676)-G-S2(689-696)-Ferritin	Extended the sequence to include a portion of S2 with the indicated leader between the two regions	PL
pCoV111	S1(12-676)-GG-S2(689-696)-Ferritin	Extended the sequence to include a portion of S2 with the indicated leader between the two regions	PL
pCoV112	S1(12-676)-PG-S2(689-696)-Ferritin	Extended the sequence to include a portion of S2 with the indicated leader between the two regions	PL
pCoV113	S1-Y312N/Q313Y/T314T-Ferritin	S1 with indicated point mutations	PL
pCoV114	S1-I651N/A653S-Ferritin	S1 with indicated point mutations	PL
pCoV115	S1-S316C/V595C-Ferritin	S1 with indicated point mutations	PL
pCoV116	S1-V320C/S591C-Ferritin	S1 with indicated point mutations	PL
pCoV117	S1-L560Q/F562H-Ferritin	S1 with indicated point mutations	PL
pCoV118	S1-F562N/Q564T-Ferritin	S1 with indicated point mutations	PL
pCoV119	S1-F490R-Ferritin	S1 with indicated point mutation	PL
pCoV120	S1-F490A-Ferritin	S1 with indicated point mutation	PL
pCoV02	S1(16-678)-Ferritin	4 residues removed from N-terminus	PL
pCoV67	His8-3C-S1-Ferritin	His8 and HRV-3C cleavage site added to N-terminus	PL

1043
1044

1045 **Table S2. Negative-stain Electron Microscopy Data Collection and Refinement**
1046

Protein	SpFN_1B-06-PL	RFN_131	pCoV146	pCoV111	pCoV1B-05
Immunogen Fused	Spike (S2P)	RBD	RBD-NTD	S1	Spike (S2P)
EMPIAR Code	XXXXX	XXXXX	XXXXX	XXXXX	XXXXX
EMDB Code	XXXX	XXXX	XXXX	XXXX	XXXX
Data Collection					
Microscope	Tecnai T20	Tecnai T20	Tecnai T20	Tecnai T20	Talos L120C
Voltage (kV)	200 kV	200 kV	200 kV	200 kV	120 kV
Camera	Eagle 4K	Eagle 4K	Eagle 4K	Eagle 4K	Ceta
Software	SerialEM	SerialEM	SerialEM	SerialEM	EPU
Pixel Size (Å/pix)	2.195	2.195	2.195	2.195	2.542
Underfocus range	0.7-1.3	0.8-1.3	0.6-1.5	0.8-1.6	0.5-0.9
Image Processing					
Software	RELION 3.0.8	RELION 3.0.8	RELION 3.0.8	RELION 3.0.8	RELION 3.1.1
# Particle Images	11502	3383	832	2121	2143
Pixel Size (Å/pixel)	4.39	4.39	4.39	4.39	5.084
Box Size (pixels)	160	160	160	160	200
Symmetry (3D)	O	O	O	O	--
Initial Lowpass (Å) (RELION)	100	80	100	100	--
High-res Limit (Å) (cisTEM)	--	--	--	--	--
Resolution (Å)	25	21	30	30	--

1047

1048 **Table S3. Mouse immunogenicity study immunogens, adjuvants, and mouse type**

pCOV no.	Immunogen design category, Study design	C57BL/6 ALFQ	Balb/c ALFQ	C57BL/6 Alhydrogel	Balb/c Alhydrogel
1B-05	S-Trimer-Ferritin	X	X		
1B-06-PL	S-Trimer-Ferritin	X	X	X	X
RBD-Ferritin constructs					
pCOV no.	Immunogen design category, Study design	C57BL/6 ALFQ	Balb/c ALFQ	C57BL/6 Alhydrogel	Balb/c Alhydrogel
50	RBD-Ferritin		X		
58	RBD-Ferritin	X	X	X	X
59	RBD-Ferritin		X		
127	RBD(57+58)-Ferritin	X	X	X	X
129	RBD(50+58)-Ferritin	X	X	X	X
130	RBD(50+59)-Ferritin		X		
131	RBD(53+58)-Ferritin	X	X	X	X
S1-Ferritin constructs					
pCOV no.		C57BL/6 ALFQ	Balb/c ALFQ	C57BL/6 Alhydrogel	Balb/c Alhydrogel
111	S1-Ferritin	X	X		
RBD-NTD-Ferritin constructs					
pCOV no.	Immunogen design category, Study design	C57BL/6 ALFQ	Balb/c ALFQ	C57BL/6 Alhydrogel	Balb/c Alhydrogel
122	RBD-NTD-Ferritin	X	X		
125	RBD(58)-NTD-Ferritin		X		X
146	RBD(53+58)-NTD-Ferritin	X	X	X	X
147	RBD(57+58)-NTD-Ferritin	X			

1049

1050 **Table S4. Animal immunogenicity SARS-CoV-2 pseudovirus neutralization ID50 and ID80**
1051 Numbers shown are the ID50/ID80 geometric mean titers for a group, with study week 2, 5, and 8 shown in vertical
1052 order.
1053

pCOV no.	Immunogen design category, Study design	C57BL/6 ALFQ	Balb/c ALFQ	C57BL/6 Alhydrogel	Balb/c Alhydrogel
1B-05	S-Trimer-Ferritin (x 2 groups)	702/189 8,709/2,346 13,076/5,647	115/<80 3,934/716 5,546/1,447		
1B-06-PL	S-Trimer-Ferritin	14,976/5,396 41,237/16,8184 7,323/16,52	1,152/355 16,816/6,662 25,062/6,540		
RBD-Ferritin constructs					
pCOV no.	Immunogen design category, Study design	C57BL/6 ALFQ	Balb/c ALFQ	C57BL/6 Alhydrogel	Balb/c Alhydrogel
50	RBD-Ferritin		X		
58	RBD-Ferritin	577/238 11,224/2,793 31,562/10,09	353/123 13,466/3,802 25,340/7,692	293/211 1,734/688 5,097/1261	232/<80 4,836/1,086 9,439/2,569
59	RBD-Ferritin		X		
127	RBD(57+58)-Ferritin	X	X	X	X
129	RBD(50+58)-Ferritin	X	X	X	X
130	RBD(50+59)-Ferritin		X		
131	RBD(53+58)-Ferritin	358/107 15,950/5,667 38,110/12,824	270/95 13,090/3,539 32,969/10,079	682/163 1,181/403 2,845/529	119/<40 182/103 240/99
S1-Ferritin constructs					
pCOV no.		C57BL/6 ALFQ	Balb/c ALFQ	C57BL/6 Alhydrogel	Balb/c Alhydrogel
111	S1-Ferritin	1,770/350 14,893/3,636 19,157/5,564	450/172 18,112/3,846 17,108/3,886		
RBD-NTD-Ferritin constructs					
pCOV no.	Immunogen design category, Study design	C57BL/6 ALFQ	Balb/c ALFQ	C57BL/6 Alhydrogel	Balb/c Alhydrogel
122	RBD-NTD-Ferritin	X	X		
125	RBD(58)-NTD-Ferritin		X		X
146	RBD(53+58)-NTD-Ferritin	230/91 16,678/4,356 20,107/6,126	240/89 31,252/7,190 24,854/6,744	<80/<80 667/460 940/289	662/<80 2,087/537 2,417/701
147	RBD(57+58)-NTD-Ferritin	X			

1054

31

Materials and Methods

Immunogen Modeling and Design

1057 Following release of the SARS-CoV-2 sequence on Jan 10th 2020, initial RBD-Ferritin and S1-Ferritin
1058 immunogens were designed (Table S1). Subsequent iterative immunogen design and optimization utilized
1059 atomic models of the SARS-CoV-2 RBD molecule (Joyce et al., 2020), or the SARS-2 S trimer structure
1060 PDB ID: 6VXX, and PDB ID: 3BVE for the *Helicobacter pylori* Ferritin, and PDB ID: 4LQH for the
1061 bullfrog linker sequence. Pymol (Schrödinger) was used to generate the ferritin 24- subunit particle, and a
1062 map created in UCSF Chimera (Pettersen et al., 2004) was supplied to cisTEM (Grant et al., 2018)
1063 "align_symmetry" to align the ferritin particle to an octahedral symmetry convention. This was supplied to
1064 "phenix.map_symmetry" to generate a symmetry file and PDB file, for octahedral (for monomer-fusions)
1065 and D4 (for trimer-fusions) symmetry. S-domain ferritin nanoparticle fusions were modelled using Pymol
1066 and Coot (Emsley et al., 2010) and expanded using "phenix.apply_ncs" (Liebschner et al., 2019). Visual
1067 analysis and figure generation was conducted using ChimeraX and PyMOL.
1068   RBD-Ferritin designs were generated by assessment of the hydrophobic surface of the SARS-CoV-
1069 2 RBD surface and determining surface accessible mutations that reduced the hydrophobic surface. S1-
1070 Ferritin designs were creating using the PDB ID: 6VXX and including a short region of the S2 domain,
1071 which interacts with S1. Spike-Ferritin designs were created by modeling the coiled-coil region between S
1072 residues 1140 and 1158 and increasing the coil-coil interaction either by mutagenesis, or by increasing the
1073 length of the interaction region. RBD-NTD-Ferritin designs utilized RBD constructs with improved
1074 properties in the context of RBD-Ferritin, which were fused to the N-terminus of NTD (12 - 303)-Ferritin
1075 by a short 6 amino-acid linker.

DNA plasmid construction and preparation

1078 SARS-CoV-2 S-domain ferritin constructs were derived from the Wuhan-Hu-1 strain genome sequence
1079 (GenBank MN9089473), to include the following domains: RBD subunit (residues 331 - 527), NTD subunit
1080 (residues 12 - 303), RBD subunit linked to NTD subunit (residues 331 - 527 linked to residues 12 - 303
1081 with a short GSG linker), S1 domain (residues 12 - 696) and S ectodomain (residues 12 – 1158). Constructs
1082 were modified to incorporate a N-terminal hexa-histidine tag (his) for purification of the RBD-Ferritin and
1083 RBD-NTD-Ferritin constructs.
1084   An S-2P construct was used as a template to generate the set of Spike ferritin nanoparticles.
1085 Subsequent designs involving small deletions, additions and point mutations were generated using a
1086 modified QuikChange site-directed mutagenesis protocol (Agilent). RBD-ferritin and S1-ferritin constructs
1087 were synthesized by GenScript. For some of the RBD-ferritin constructs, gene segments (gBlocks) were
1088 synthesized by Integrated DNA Technologies to encode various linker regions between RBD and ferritin.
1089 Gene segments were stitched together with RBD- and ferritin-encoding PCR products using overlap
1090 extension PCR and were re-subcloned into the CMVR vector. The His-tagged SARS-CoV-2 RBD molecule
1091 was generated by amplifying the RBD domain from the RBD-Ferritin plasmid while encoding the 3'
1092 purification tag and subcloned into the CMVR vector. The NTD protein subunit was generated in a similar
1093 manner, by amplifying the NTD domain from the S1-Ferritin construct. For expression of S, RBD, and
1094 NTD proteins, the S protein domains were cloned into the CMVR expression plasmid using the
1095 NotI/BamHI restriction sites. Constructs including the N-terminal region of the S protein included the native
1096 leader sequence; for constructs not including this region we utilized a prolactin leader (PL) sequence
1097 (Boyington et al., 2016).
1098   Plasmid DNA generated by subcloning (restriction digest and ligation) was amplified in and
1099 isolated from E. coli Top10 cells. The constructs resulting from site-directed mutagenesis were either
1100 amplified in and isolated from E. coli Stbl3 or Top10 cells. Large-scale DNA isolation was performed using
1101 either endo free Maxiprep, Megaprep or Gigaprep kits (Qiagen).

Immunogen expression and purification

1104 All expression vectors were transiently transfected into Expi293F cells (Thermo Fisher Scientific)
1105 using ExpiFectamine 293 transfection reagent (Thermo Fisher Scientific). Cells were grown in

1106   polycarbonate baffled shaker flasks at 34°C or 37°C and 8% CO_2 at 120 rpm. Cells were harvested 5-6 days
1107   post-transfection via centrifugation at 3,500 x g for 30 minutes. Culture supernatants were filtered with a
1108   0.22-µm filter and stored at 4 ºC prior to purification.
1109   His-tagged proteins were purified using Ni-NTA affinity chromatography, while untagged proteins
1110   were purified with GNA lectin affinity chromatography. Briefly, 25 mL GNA-lectin resin (VectorLabs)
1111   was used to purify untagged protein from 1L of expression supernatant. GNA resin was equilibrated with
1112   10 column volumes (CV) of phosphate buffered saline (PBS) (pH 7.4) followed by supernatant loading
1113   twice at 4 ºC. Unbound protein was removed by washing with 20 CV of PBS buffer. Bound protein was
1114   eluted with 250mM methyl-α -D mannopyranoside in PBS buffer (pH 7.4). His-tagged proteins were
1115   purified using Ni-NTA affinity chromatography. 1 mL Ni-NTA resin (Thermo Scientific) was used to
1116   purify protein from 1L of expression supernatant. Ni-NTA resin was equilibrated with 5 CV of phosphate
1117   buffered saline (PBS) (pH 7.4) followed by supernatant loading 2x at 4 ºC. Unbound protein was removed
1118   by washing with 200 CV of PBS, followed by 50 CV 10mM imidazole in PBS. Bound protein was eluted
1119   with 220mM imidazole in PBS. For all proteins, purification purity was assessed by SDS-PAGE. RBD-
1120   Ferritin nanoparticle constructs had a propensity to form soluble or insoluble aggregates which affected the
1121   ability to concentrate the samples. Addition of 1mM EDTA and 5% glycerol to the NiNTA purified
1122   material, prior to SEC or other concentration steps, mitigated the aggregation issue, and increased the
1123   nanoparticle formation as judged by SEC, and confirmed by neg-EM. All proteins were further purified by
1124   size-exclusion chromatography using a 16/60 Superdex-200 purification column. Purification purity for all
1125   the proteins was assessed by SDS-PAGE. Removal of the His-tags for SARS2-CoV-2 S-2P and RBD for
1126   use in ELISA were carried out using HRV-3C protease. Endotoxin levels for ferritin nanoparticle
1127   immunogens were assessed (Endosafe® nexgen-PTS, Charles River Laboratories) and 5 % v/v glycerol
1128   was added prior to filter-sterilization with a 0.22-µm filter, flash-freezing in liquid nitrogen, and storage at
1129   -80 ºC. Ferritin nanoparticle formation was assessed by dynamic light scattering (DLS) by determining the
1130   hydrodynamic diameter at 25 °C using a Malvern Zetasizer Nano S (Malvern, Worcestershire, UK)
1131   equipped with a 633-nm laser.
1132   For the antibodies, plasmids encoding heavy and light chains of antibodies (CR3022, and SR1-
1133   SR5) were co-transfected into Expi293F cells (ThermoFisher) according to the manufacturer's instructions
1134   for expression of antibodies. After 5 days, antibodies were purified from cleared culture supernatants with
1135   Protein A agarose (ThermoFisher) using standard procedures, buffer was exchanged to PBS by dialysis,
1136   and antibody concentration was quantified using calculated extinction coefficient and A280 measurements.
1137
1138   *Negative-stain Electron Microscopy*
1139   Purified proteins were deposited at 0.02-0.08 mg/ml on carbon-coated copper grids and stained with 0.75%
1140   uranyl formate. Grids were imaged using a FEI T20 operating at 200 kV with an Eagle 4K CCD using
1141   SerialEM or using a Thermo Scientific Talos L120C operating at 120 kV with Thermo Scientific Ceta using
1142   EPU. All image processing steps were done using RELION 3.0.8, RELION 3.1.1, and/or cisTEM-1.0.0-
1143   beta. Particles were picked either manually or using templates generated from manually picked 2D class
1144   averages. CTF estimation was done with CTFFIND 4.1.13 and used for 2D classification. 3D
1145   reconstructions were generated using an initial reference generated from a corresponding synthetic atomic
1146   model with a low pass filter of 80-100 angstroms to remove distinguishable features or from a similar
1147   construct also low pass filtered to 80-100 angstroms. For all 3D reconstructions, O symmetry was enforced,
1148   and no explicit mask was used. Visual analysis and figure generation was conducted using Chimera and
1149   ChimeraX.
1150
1151   *Dynamic Light Scattering*
1152   Spike-domain ferritin nanoparticle hydrodynamic diameter was determined at 25°C using a Malvern
1153   Zetasizer Nano S (Malvern, Worcestershire, UK) equipped with a 633-nm laser. Samples were assessed
1154   accounting for the viscosity of their respective buffers.
1155
1156   *Octet Biolayer Interferometry binding and ACE2 inhibition assays*

33

1157 All biosensors were hydrated in PBS prior to use. All assay steps were performed at 30°C with agitation
1158 set at 1,000 rpm in the Octet RED96 instrument (FortéBio). Biosensors were equilibrated in assay buffer
1159 (PBS) for 15 seconds before loading of IgG antibodies (30 µg/ml diluted in PBS). SARS-COV-2 antibodies
1160 were immobilized onto AHC biosensors (FortéBio) for 100 seconds, followed by a brief baseline in assay
1161 buffer for 15 s. Immobilized antibodies were then dipped in various antigens for 100-200 s followed by
1162 dissociation for 20-100 s.
1163   Mouse sera binding to the SARS-CoV-2 RBD, VoC RBDs, or SARS-CoV-1 RBD were carried out
1164 as follows. HIS1K biosensors(FortéBio) were equilibrated in assay buffer for 15 s before loading of His-
1165 tagged RBD (30 µg/ml diluted in PBS) for 120 seconds. After briefly dipping in assay buffer (15 seconds
1166 in PBS), the biosensors were dipped in mouse sera (100-fold dilution) for 180 seconds followed by
1167 dissociation for 60 seconds.
1168   SARS-CoV-2 and SARS-CoV-1 RBD hACE2 inhibition assays were carried out as follows. SARS-
1169 CoV-2 or SARS-CoV-1 RBD (30 µg/ml diluted in PBS) was immobilized on HIS1K biosensors (FortéBio)
1170 for 180 seconds followed by baseline equilibration for 30 s. Serum was allowed to occur for 180 s followed
1171 by baseline equilibration (30 s). ACE2 protein (30 µg/ml) was the allowed to bind for 120 s. Percent
1172 inhibition (PI) of RBD binding to ACE2 by serum was determined using the equation: $PI = 100 - [(ACE2$
1173 $binding\ in\ the\ presence\ of\ mouse\ serum)) / (mouse\ serum\ binding\ in\ the\ absence\ of\ competitor\ mAb)] \times$
1174 100.
1175
1176 *Mouse immunization*
1177 All research in this study involving animals was conducted in compliance with the Animal Welfare Act,
1178 and other federal statutes and regulations relating to animals and experiments involving animals and
1179 adhered to the principles stated in the Guide for the Care and Use of Laboratory Animals, NRC Publication,
1180 1996 edition. The research protocol was approved by the Institutional Animal Care and Use Committee of
1181 WRAIR. BALB/c and C57BL/6 mice were obtained from Jackson Laboratories (Bar Harbor, ME). Mice
1182 were housed in the animal facility of WRAIR and cared for in accordance with local, state, federal, and
1183 institutional policies in a National Institutes of Health American Association for Accreditation of
1184 Laboratory Animal Care-accredited facility.
1185   C57BL/6 or BALB/c mice (n=10/group) were immunized intramuscularly with 10 µg of
1186 immunogen (unless stated) adjuvanted with either ALFQ or Alhydrogel® in alternating caudal thigh
1187 muscles three times, at 3-week intervals; blood was collected 2 weeks before the first immunization, the
1188 day of the first immunization, and 2 weeks following each immunization, and at week 10 (Table S1). For
1189 immunogen SpFN_1B-06-PL, mice were immunized with reduced doses of protein adjuvanted with ALFQ
1190 with immunization schedule, site of injections, and timing of bleeds as described. Mice were randomly
1191 assigned to experimental groups and were not pre-screened or selected based on size or other gross physical
1192 characteristics. Serum was stored at 4°C or -80°C until analysis. Antibody responses were analyzed by
1193 Octet Biolayer Interferometry, enzyme-linked immunosorbent assay (ELISA), pseudovirus neutralization
1194 assay, and live-virus neutralization assay.
1195
1196 *Immunogen-Adjuvant preparation*
1197 Purified research grade nanoparticle immunogens were formulated in PBS with 5% glycerol at 1 mg/ml
1198 and subsequently diluted with dPBS (Quality Biological) to provide 10 µg or lower amount per 50 µl dose
1199 upon mixing with adjuvant. ALFQ (1.5X) liposomes, containing 600 µg/mL 3D-PHAD and 300 µg ug/mL
1200 QS-21, were gently mixed by slow speed vortex prior to use. Antigen was added to the ALFQ, vortexed at
1201 a slow speed for 1 minute, mixed on a roller for 15 minutes, and stored at 4°C for 1 h prior to immunization.
1202 Spike-Ferritin nanoparticle immunogens were formulated with ALFQ to contain 20 µg 3D-PHAD and 10
1203 µg QS21 per 50 µl dose. Alhydrogel® stock (10 mg/ml aluminum (GMP grade; Brenntag)) was diluted to
1204 900 µg/mL (1.5X) with DPBS and gently mixed. Appropriate volume and concentration of antigen was
1205 added to the diluted Alhydrogel® before being vortexed at low speed for 1 min, mixed on a roller for 15
1206 minutes, and stored at 4°C for at least 1 h prior to immunization. Spike-Ferritin nanoparticle immunogens
1207 were adsorbed to Alhydrogel® aluminum hydroxide at 30 µg aluminum per 50 µl dose.

Enzyme Linked Immunosorbent Assay (ELISA)

96-well Immulon "U" Bottom plates were coated with 1 μg/mL of RBD or S protein (S-2P) antigen in PBS, pH 7.4. Plates were incubated at 4°C overnight and blocked with blocking buffer (Dulbecco's PBS containing 0.5% milk and 0.1% Tween 20, pH 7.4, at room temperature (RT) for 2 h. Individual serum samples were serially diluted 2-fold in blocking buffer and added to triplicate wells and the plates were incubated for 1 hour (h) at RT. Horseradish peroxidase (HRP)-conjugated sheep anti-mouse IgG, gamma chain specific (The Binding Site) was added and incubated at RT for an hour, followed by the addition of 2,2'-Azinobis [3-ethylbenzothiazoline-6-sulfonic acid]-diammonium salt (ABTS) HRP substrate (KPL) for 1 h at RT. The reaction was stopped by the addition of 1% SDS per well and the absorbance (A) was measured at 405 nm (A405) using an ELISA reader Spectramax (Molecular Devices, San Jose, CA)) within 30 min of stopping the reaction.. Antibody positive (anti-RBD mouse mAb; BEI resources) and negative controls were included on each plate. The results are expressed as end point titers, defined as the reciprocal dilution that gives an absorbance value that equals twice the background value (antigen-coated wells that did not contain the test sera, but had all other components added).

Mouse isotype ELISA were performed using a similar approach as above, but with the following differences. Only Spike protein (S-2P) was used to coat the wells. The plates were blocked with PBS containing 0.2% bovine serum albumin (BSA), pH 7.4 for 30 minutes. The mouse serum samples were serially diluted in duplicates either 3- or 4-fold in PBS containing 0.2% BSA and 0.05% Tween 20, pH7.4. The secondary antibodies were HRP-conjugated AffiniPure Goat Anti-Mouse antibodies from Jackson ImmunoResearch specific for either Fcγ subclass 1, Fcγ subclass 2a, or Fcγ subclass 2c. The secondary antibodies were incubated for 30 minutes. TMB (3,3',5,5'-Tetramethylbenzidine) substrate (Thermo) was added and the plates were incubated at RT for 5-10 minutes to allow color development. Stop solution (Thermo) was added and the A405 was measured using a VersaMax microplate reader (Molecular Devices). A titration curve of serum concentration versus A450 was created. The titration curves were interpolated to determine the dilution factor where A450=1.0 for each mouse sera sample and IgG subclass, and the resulting values were used to calculate the IgG1/IgG2a ratio (for BALB/c mice) or IgG1/IgG2c ratio (for C57BL/6 mice). In the animal groups immunized with SpFN_1B-06-PL with the adjuvant Alhydrogel®, many of the mouse IgG usage ratio could not be calculated due to insufficient signal for either IgG2a or IgG2c in the mouse sera.

SARS-CoV-2 and SARS-CoV-1 pseudovirus neutralization assay

The S expression plasmid sequences for SARS-CoV-2 (Wuhan1, B.1.1.7, and B.1.351) and SARS-CoV were codon optimized and modified to remove an 18 amino acid endoplasmic reticulum retention signal in the cytoplasmic tail in the case of SARS-CoV-2, and a 28 amino acid deletion in the cytoplasmic tail in the case of SARS-CoV. This allowed increased S incorporation into pseudovirions (PSV) and thereby enhance infectivity. Virions pseudotyped with the vesicular stomatitis virus (VSV) G protein were used as a non-specific control. SARS-CoV-2 pseudovirions (PSV) were produced by co-transfection of HEK293T/17 cells with a SARS-CoV-2 S plasmid (pcDNA3.4) and an HIV-1 NL4-3 luciferase reporter plasmid (The reagent was obtained through the NIH HIV Reagent Program, Division of AIDS, NIAID, NIH: Human Immunodeficiency Virus 1 (HIV-1) NL4-3 ΔEnv Vpr Luciferase Reporter Vector (pNL4-3.Luc.R-E-), ARP-3418, contributed by Dr. Nathaniel Landau and Aaron Diamond). The SARS-CoV-2 S expression plasmid sequence was derived from the Wuhan seafood market pneumonia virus isolate Wuhan-Hu-1, complete genome (GenBank accession MN908947), and the SARS-CoV-1 expression plasmid was derived from the Urbani S sequence.

1253   Infectivity and neutralization titers were determined using ACE2-expressing HEK293 target cells
1254   (Integral Molecular) in a semi-automated assay format using robotic liquid handling (Biomek NXp
1255   Beckman Coulter). Test sera were diluted 1:40 in growth medium and serially diluted, then 25 µL/well was
1256   added to a white 96-well plate. An equal volume of diluted SARS-CoV-2 PSV was added to each well and
1257   plates were incubated for 1 hour at 37°C. Target cells were added to each well (40,000 cells/ well) and
1258   plates were incubated for an additional 48 hours. RLUs were measured with the EnVision Multimode Plate
1259   Reader (Perkin Elmer, Waltham, MA) using the Bright-Glo Luciferase Assay System (Promega
1260   Corporation, Madison, WI). Neutralization dose–response curves were fitted by nonlinear regression with
1261   a five-parameter curve fit using the LabKey Server® (Piehler et al., 2011), and the final titers are reported
1262   as the reciprocal of the dilution of serum necessary to achieve 50% neutralization (ID50, 50% inhibitory
1263   dilution) and 80% neutralization (ID80, 80% inhibitory dilution). Assay equivalency for SARS-CoV-2 was
1264   established by participation in the SARS-CoV-2 Neutralizing Assay Concordance Survey (SNACS) run by
1265   the Virology Quality Assurance Program and External Quality Assurance Program Oversite Laboratory
1266   (EQAPOL) at the Duke Human Vaccine Institute, sponsored through programs supported by the National
1267   Institute of Allergy and Infectious Diseases, Division of AIDS.

1268

1269   *SARS-CoV-2 authentic virus neutralization assay*
1270   The neutralization assay has been described in detail previously (Case et al., 2020). Briefly, SARS-CoV-2
1271   strain 2019-nCoV/USA_WA1/2020 was obtained from the Centers for Disease Control and Prevention.
1272   Virus was passaged once in Vero CCL81 cells (ATCC) and titrated by focus-forming assay on Vero E6
1273   cells. Mouse sera were serially diluted and incubated with 100 focus-forming units of SARS-CoV-2 for 1
1274   h at 37°C. Serum-virus mixtures were then added to Vero E6 cells in 96-well plates and incubated for 1 h
1275   at 37°C. Cells were overlayed with 1% (w/v) methylcellulose in MEM. After 30 h, cells were fixed with
1276   4% PFA in PBS for 20 minutes at room temperature then washed and stained overnight at 4°C with 1 µg/ml
1277   of CR3022 (ter Meulen et al., 2006; Tian et al., 2020) in PBS supplemented with 0.1% saponin and 0.1%
1278   bovine serum albumin. Cells were subsequently stained with HRP-conjugated goat anti-human IgG for 2 h
1279   at room temperature. SARS-CoV-2-infected cell foci were visualized with TrueBlue peroxidase substrate
1280   (KPL) and quantified using ImmunoSpot® microanalyzer (Cellular Technologies, Shaker Heights, OH).
1281   Neutralization curves were generated using Prism software (GraphPad Prism 8.0).

1282

1283

1284   *Protection experiments in K18-hACE2 transgenic mice*
1285   All research in this study involving animals was conducted in compliance with the Animal Welfare Act,
1286   and other federal statutes and regulations relating to animals and experiments involving animals and
1287   adhered to the principles stated in the Guide for the Care and Use of Laboratory Animals, NRC Publication,
1288   1996 edition. The research protocol was approved by the Institutional Animal Care and Use Committee of
1289   the Trudeau Insiture. K18-hACE2 transgenic mice were obtained from Jackson Laboratories (Bar Harbor,
1290   ME). Mice were housed in the animal facility of the Trudeau Institute and cared for in accordance with
1291   local, state, federal, and institutional policies in a National Institutes of Health American Association for
1292   Accreditation of Laboratory Animal Care-accredited facility.
1293   To determine an appropriate challenge viral stock amount and establish the K18-hACE2 SARS-
1294   CoV-2 mouse challenge model, five viral doses were used to inoculate the K18-hACE2 mice. Each study
1295   group was composed of 10 hACE2 K18 Tg mice (5 males and 5 females). Mice were infected on study day
1296   0 doses ranging from 5×10^2 to 1×10^5 PFU of SARS-CoV-2 USA-WA1/2020 administered via intranasal
1297   instillation. All mice were monitored for clinical symptoms and body weight twice daily, every 12 hours,
1298   from study day 0 to study day 14. Mice were euthanized if they displayed any signs of pain or distress as
1299   indicated by the failure to move after stimulated or inappetence, or if mice have greater than 25% weight
1300   loss compared to their study day 0 body weight. Hematoxylin and eosin staining of lung sections following
1301   infection with 1.25×10^4 PFU compared to control uninfected mouse lung sections are shown in Figure S6.

36

1302   For the passive immunization study, on day -1, K18-hACE2 mice were injected intravenously with
1303 purified IgG from C57BL/6 vaccinated mice. On study day 0, all mice were inoculated with 1.25×10^4 PFU
1304 of SARS-CoV-2 USA-WA1/2020 via intranasal instillation. All mice were monitored for clinical
1305 symptoms and body weight twice daily, every 12 hours, from study day 0 to study day 14. Mice were
1306 euthanized if they displayed any signs of pain or distress as indicated by the failure to move after stimulated
1307 or inappetence, or if mice have greater than 25% weight loss compared to their study day 0 body weight.
1308
1309 *Data Analysis*
1310 Data analyses used GraphPad (San Diego, CA) Prism software and statistical tests as described for
1311 individual experiments.
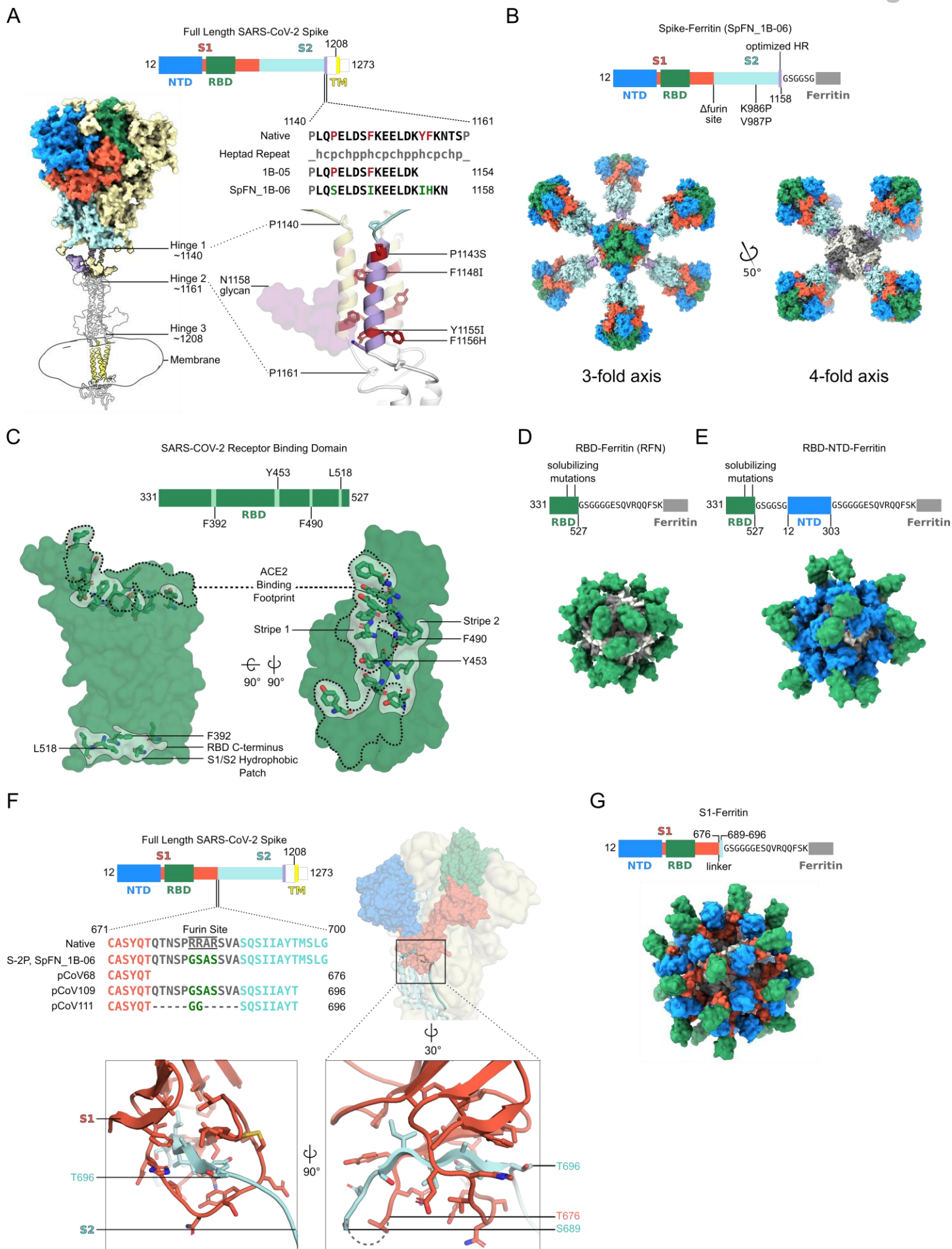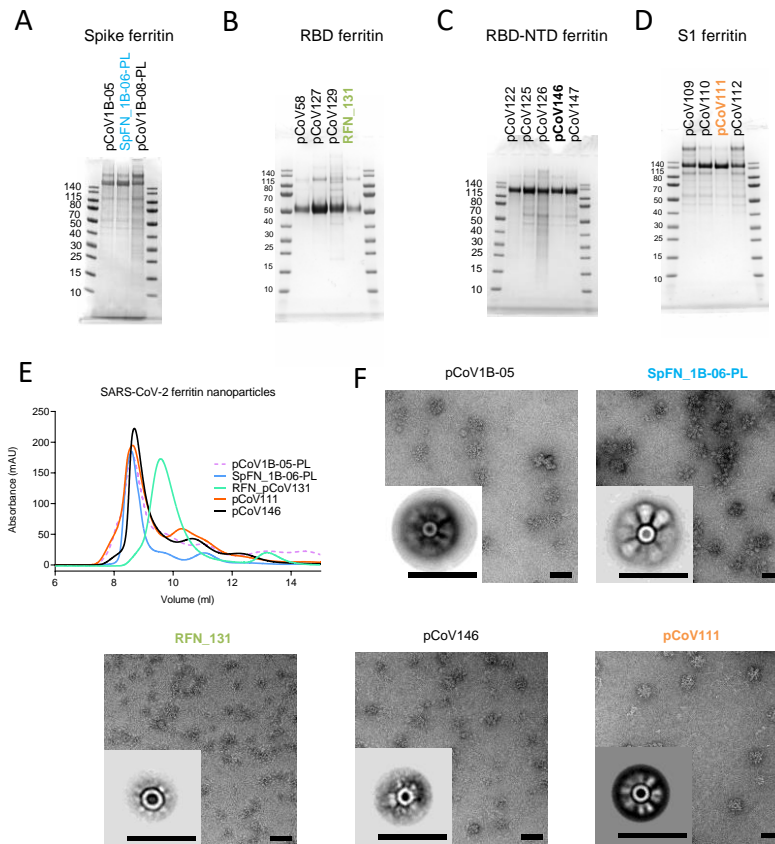
Figure 1

Figure 2

Figure 2. Biophysical characterization of SARS-CoV-2 S-based ferritin nanoparticle vaccine candidates
SDS-PAGE of (A) Spike ferritin nanoparticles, (B) RBD ferritin nanoparticles, (C) S1 ferritin nanoparticle, and (D) RBD-NTD ferritin nanoparticles. Molecular weight standards are indicated in kDa.
(E) Size-exclusion chromatography on a Superdex S200 10/300 column of representative SARS-CoV-2 S-based ferritin nanoparticles.
(F) Negative-stain electron microscopy 2D class averages of purified nanoparticles. The black bars represent 50 nm.
See also Figure S2 and S3.
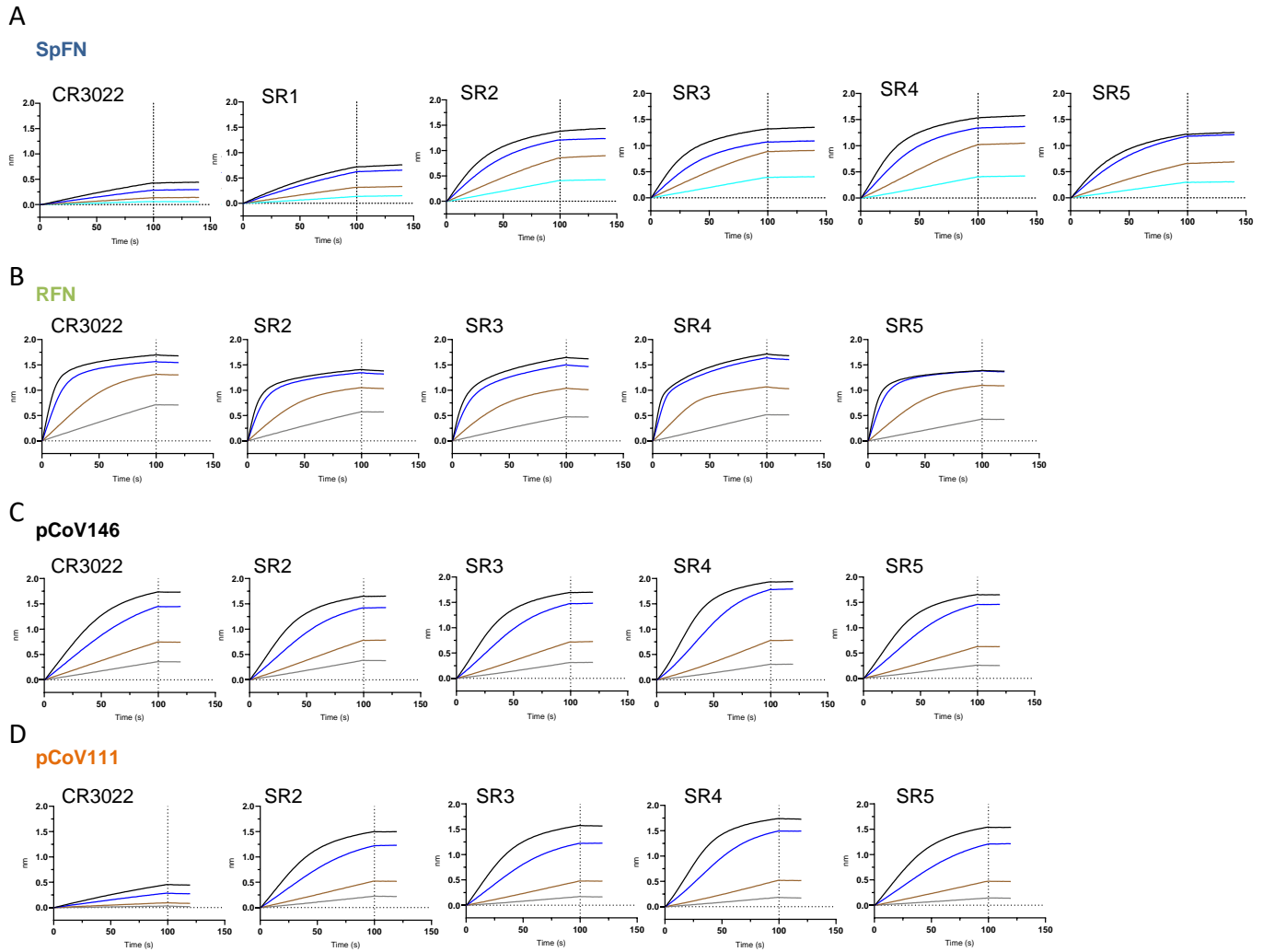
Figure 3

Figure 3. Antigenic characterization of select SARS-CoV-2 S-based ferritin nanoparticle vaccine candidates
Binding response of SARS-CoV-2 neutralizing antibodies to each of the lead candidates from the four design categories measured by biolayer interferometry with two-fold serial dilution of each antibody starting at 30 µg/ml.
(A) Spike ferritin nanoparticle SpFN (pCoV1B-06-PL).
(B) RBD ferritin RFN (pCoV131).
(C) RBD-NTD ferritin nanoparticle pCoV146.
(D) S1 ferritin nanoparticle pCoV111.
See also Figure S3.
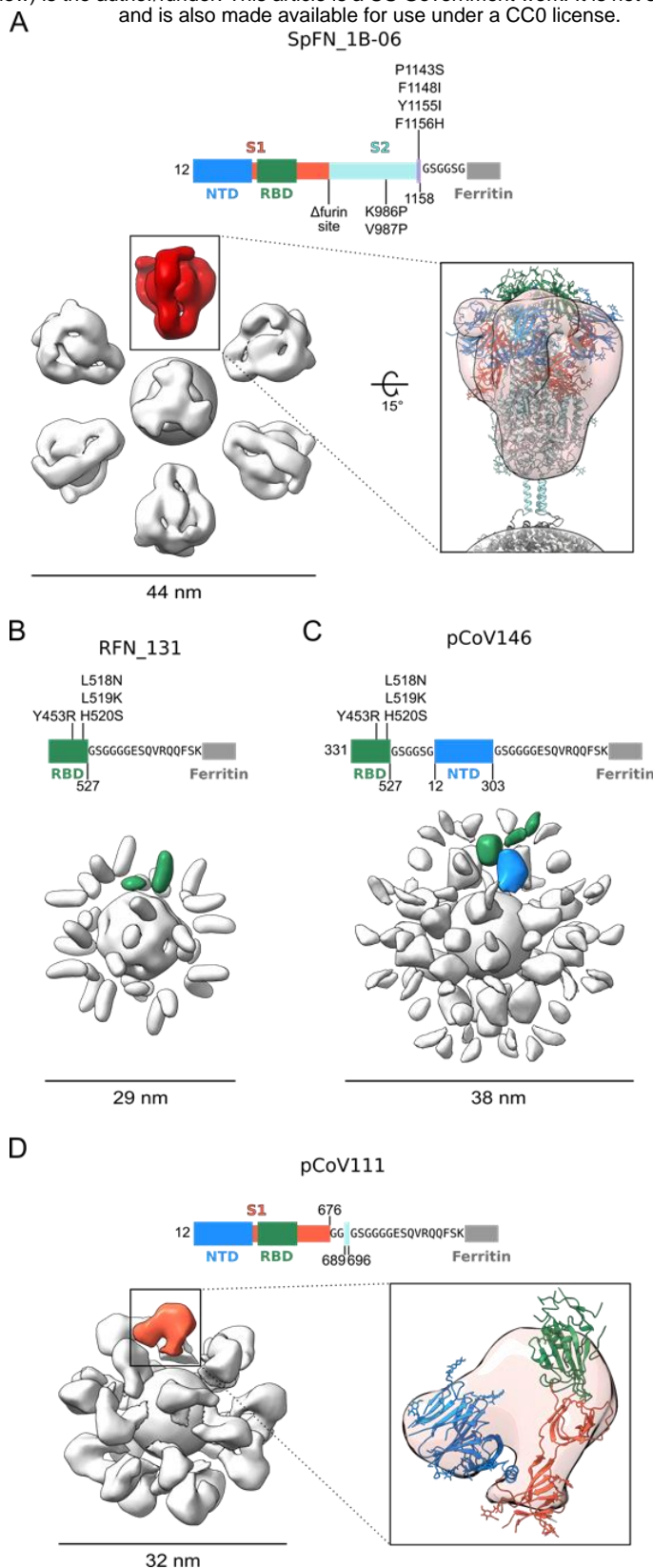
Figure 4. Negative-Stain Electron Microscopy 3D Reconstructions of SARS-CoV-2 S-based ferritin nanoparticles

Modifications made to native sequence and linkers used for each construct are shown in schematic diagrams.

(A) Negative-stain 3D reconstructions with applied octahedral symmetry are shown with an asymmetric unit of non-ferritin density colored and the size of each particle indicated in nanometers. Spike trimer density, is colored in red, and a model of a SARS-CoV-2 trimer based on PDB 6VXX is shown docked into the negative-stain map and colored according to the sequence diagram.

(B) Two non-ferritin densities per asymmetric unit were observed for RFN and are highlighted in green. These densities putatively correspond to the receptor-binding domain (RBD) but lack low resolution distinguishing features due to the small, globular shape of these domains. The presence of two densities is likely due to flexibility in the linker and heterogeneity in the RBD pose.

(C) Two layers of densities were distinguishable for pCoV146, with the putative N-terminal domain (NTD) density of an asymmetric unit colored blue, proximal to the ferritin and two smaller, more flexible densities corresponding to RBD distal to the ferritin and colored green.

(D) An asymmetric unit of non-ferritin density for pCoV111 is colored in orange and a monomer of S1 in the closed trimer state from PDB 6VXX is shown docked into the density with domains colored as in the sequence diagram.
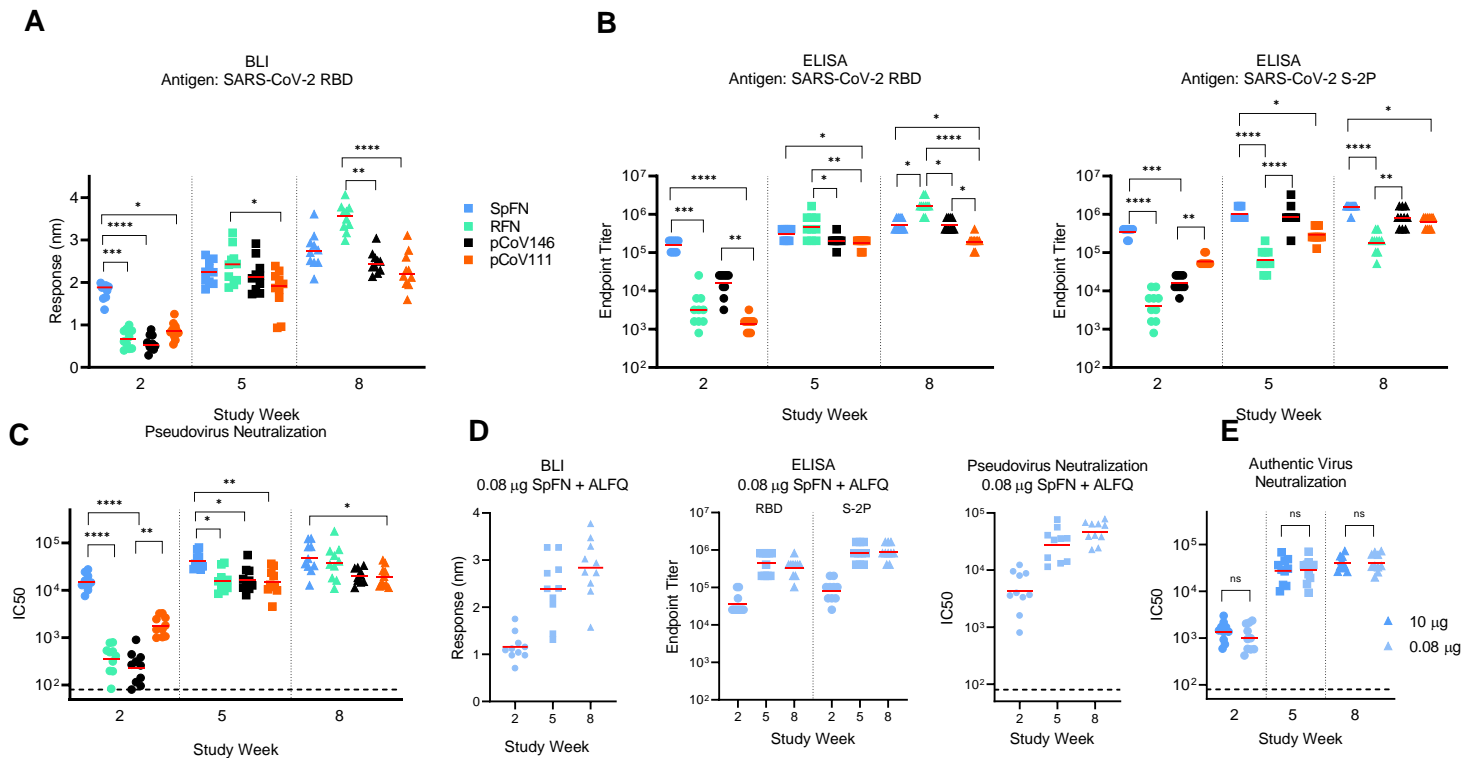
See also Figure S2 and Table S2

Figure 5

Figure 5 SARS-CoV-2 S-domain nanoparticle vaccine candidates elicit robust binding and neutralizing antibody responses in C57BL/6 mice.

Data relating to each category of immunogen are colored as follows: SpFN (blue), RFN (green), pCoV146 (black) and pCoV111 (orange). N= 10/group.

(A) Biolayer interferometry binding of mouse sera to SARS-COV-2 RBD. Study week is indicated on the base of the graph. Mean value is indicated by a horizontal line. Statistical comparison at each timepoint was carried out using a a Kruskal-Wallis test followed by a Dunn's post-test.

(B) ELISA binding of mouse sera to SARS-COV-2 S-2P or RBD. Study week is indicated on the base of the graph. Geometric mean value is indicated by a horizontal line. Statistical comparison at each timepoint was carried out using a a Kruskal-Wallis test followed by a Dunn's post-test.

(C) SARS-CoV-2 pseudovirus neutralization ID50 and ID80 values. Geometric mean value is indicated by a horizontal line. Statistical comparisons at each given timepoint was carried out using a Kruskal-Wallis test followed by a Dunn's post-test.

(D) Binding and pseudovirus neutralization of sera from mice immunized with 0.08 μg SpFN + ALFQ.

(E) Authentic SARS-CoV-2 virus neutralization ID50 and ID80 are shown for mice immunized with 10 μg (blue) or 0.08 μg (light blue) SpFN + ALFQ. Geometric mean titer is indicated by a horizontal line. Comparisons between dose group at each time point were carried out using a Mann-Whitney unpaired two-tailed non-parametric test.

In panels A – C, all groups at a given study timepoint were compared to each other. Only groups with significant differences are indicated by a bar; all other groups did not show statistically significant differences. P values <0.0001 (****), <0.001 (***), <0.01 (**), or <0.05 (*).
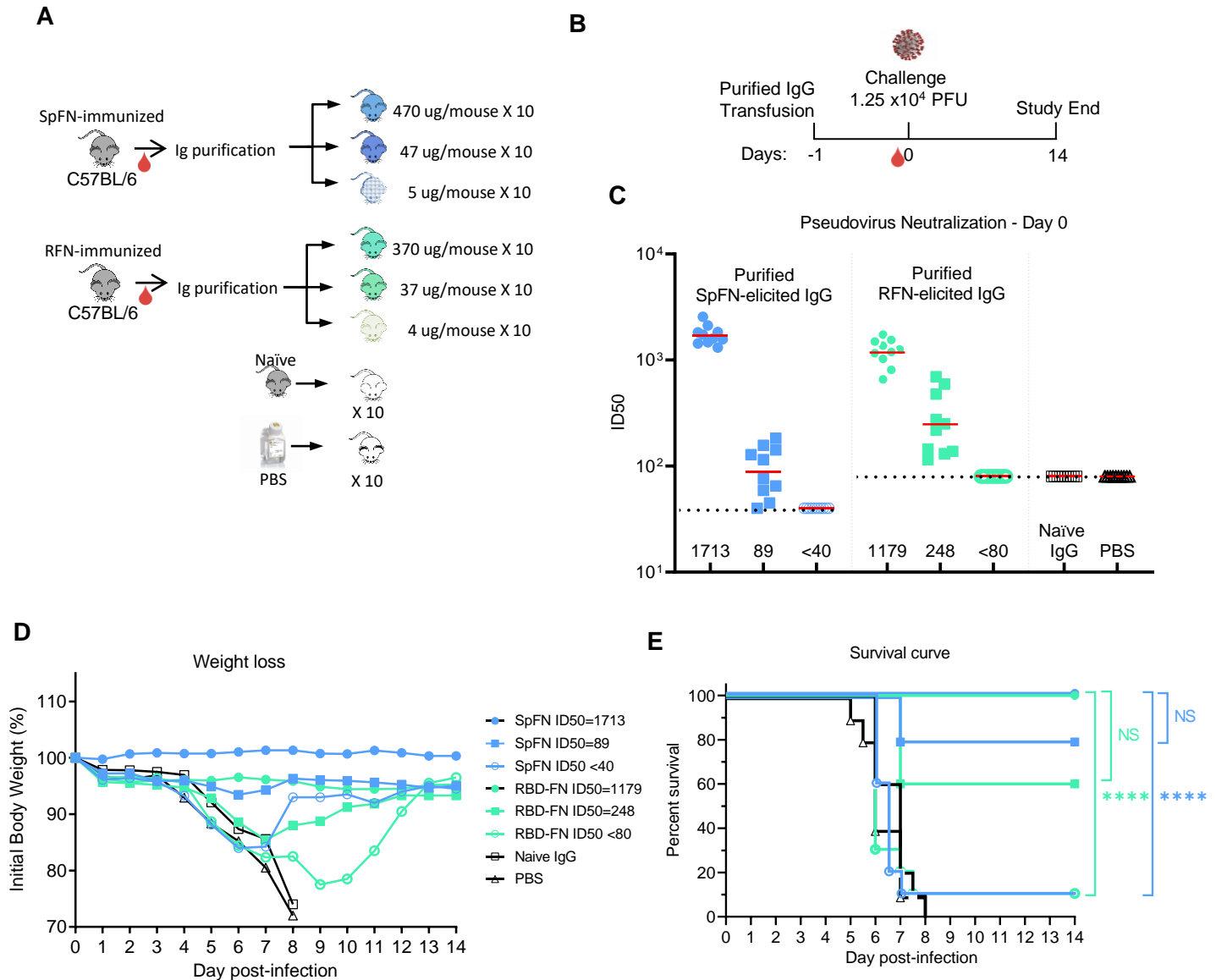
See also Figure S4 and S5, and Table S3 and S4.

Figure 6

Figure 6. SpFN- and RFN- protective immunity in K18-hACE2 transgenic mice.

(A) IgG was purified from SPFN- or RFN-vaccinated mouse sera and passively transferred at specific IgG amounts ranging from 4 - 470 μg/mouse in a final volume of 200 μl. Control naïve mouse IgG was formulated at 2 mg/ml. (n=10/group, 5 female, 5 male).

(B) Mouse challenge study schematic. K18-hACE2 mice (n=10/group, 5 female, 5 male) received control IgG (black), PBS (gray), and purified IgG, one day prior to challenge with 1.25×10^4 PFU of SARS-CoV-2.

(C) SARS-CoV-2 pseudovirus neutralization ID_{50} titers of mouse sera at study day 0.

(D) Percentage of initial weight of K18-hACE2 mice for the 8 study groups. Legend is shown in panel **E**.

(E) Survival curves of K18-hACE2 mice with groups indicated based on animal vaccination group and the pseudovirus ID_{50} neutralization values. Statistical comparisons were carried out using Mantel-Cox test followed by Bonferroni correction.
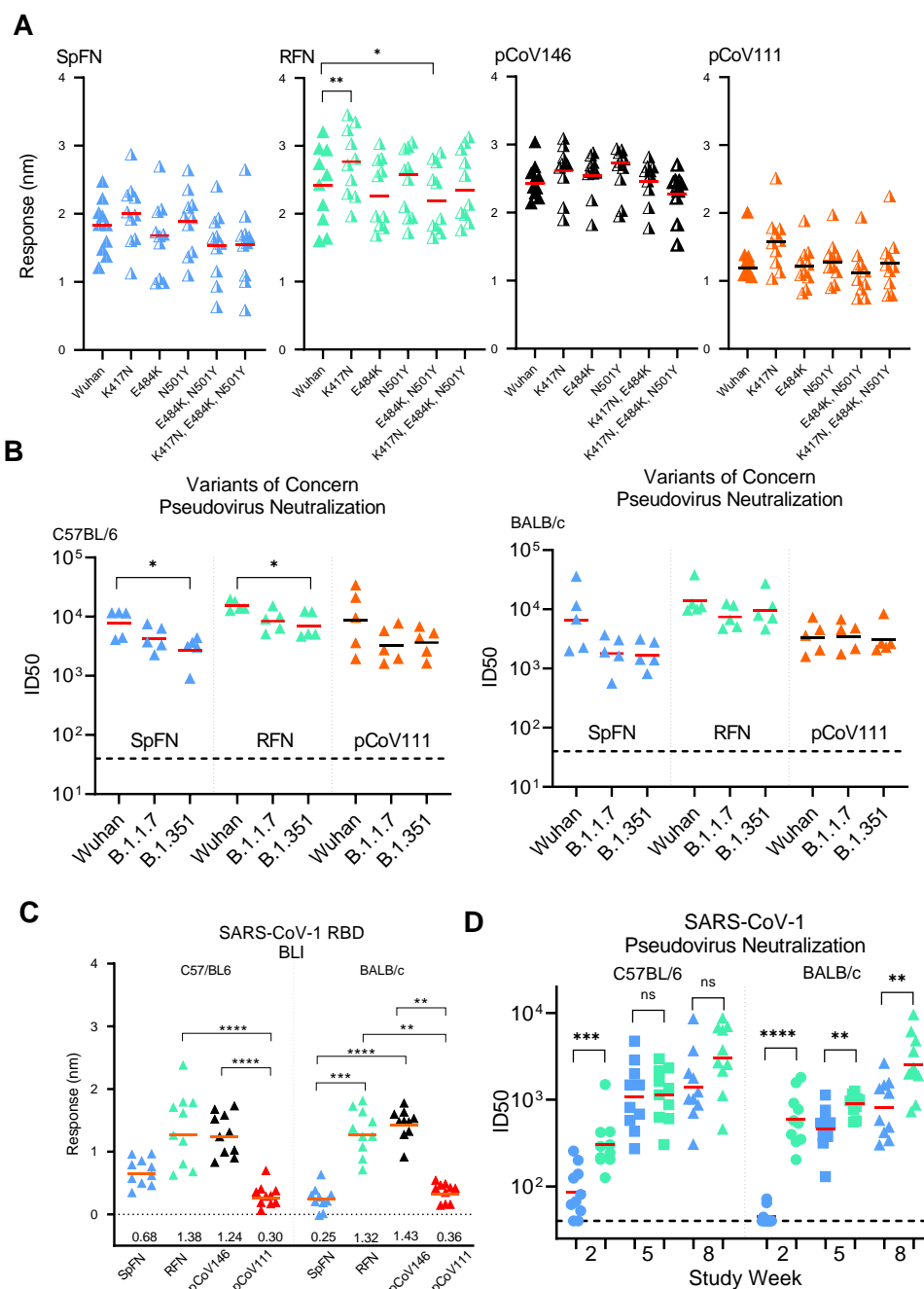
See also Figure S6.

Figure 7

Figure 7. SARS-CoV-2 S-domain nanoparticle vaccine candidates elicit robust antibody binding responses and neutralizing activity against SARS-CoV-2 VoC and SARS-CoV-1.

(A) Biolayer Interferometry binding of study week 10 immunized C57BL/6 mouse serum to SARS-CoV-2 RBD, and SARS-CoV-2 RBD variants. Immunogens are indicated at the top left of each graph. Mean values are indicated by a horizontal line, n=10, Significance was assessed using a Kruskal-Wallis test followed by a Dunn's post-test.

(B) Pseudovirus neutralization (ID_{50} values) of study week 10 immunized C57BL/6 and BALB/c mouse serum to SARS-CoV-2 Wuhan-1, B.1.1.7, and B.1.351 pseudotyped viruses. Immunogens are indicated at the base of each graph. Geometric mean values are indicated by a horizontal line, n=5, statistical significance for each immunogen was assessed using a Kruskal-Wallis test followed by a Dunn's post-test.

(C) Biolayer Interferometry binding of study week 10 immunized C57BL/6 and BALB/c mouse serum to SARS-CoV-1 RBD. Immunogens are indicated at the base of each graph. Mean values are indicated by a horizontal line, n=10, statistical significance was assessed using a Kruskal-Wallis test followed by a Dunn's post-test.

(D) Pseudovirus neutralization (ID_{50} values) of study week 10 immunized C57BL/6 and BALB/c mouse serum to SARS-CoV-1 Urbani strain pseudotyped viruses. Data related to SpFN and RFN are colored blue and green respectively. Statistical comparisons between SpFN and RFN responses at each time point were carried out using a Mann-Whitney unpaired two-tailed non-parametric test.

Immunogens are indicated at the base of each graph. Geometric mean values are indicated by a horizontal line, n=10, P values <0.0001 (****), <0.01 (**) or <0.05 (*).
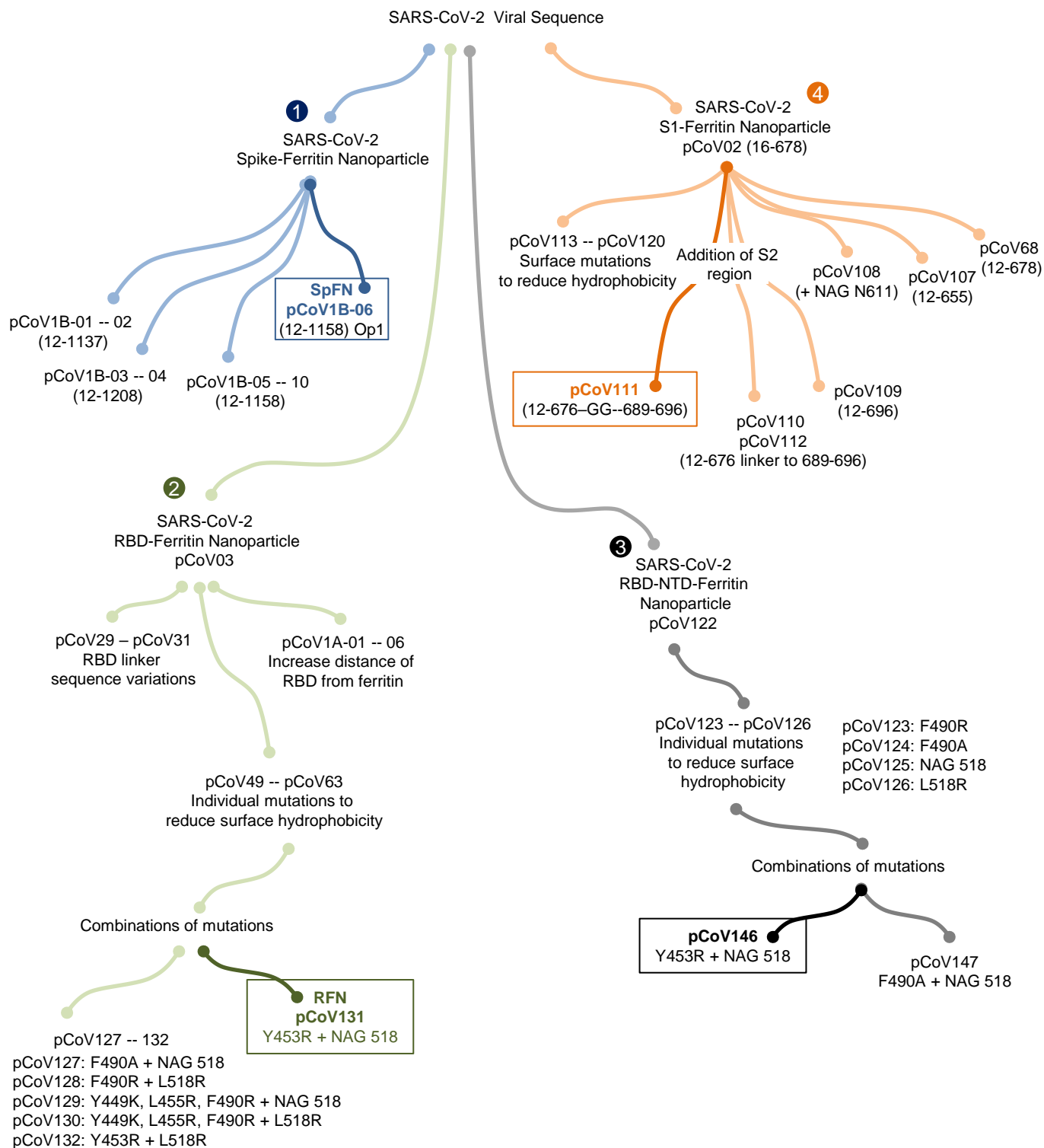
See also Figure S4 and S5.

Figure S1. Structure-based design of SARS-CoV-2 S-domain ferritin nanoparticle immunogens and design pipeline. Related to Figure 1.

Four ferritin nanoparticle immunogen designs were developed focused on (1) Spike ferritin nanoparticles (blue), (2) RBD ferritin nanoparticles (green), (3) RBD-NTD ferritin nanoparticles (black), and (4) S1 ferritin nanoparticles (orange). The design iterations and concepts are indicated, along with select mutations and design name. Lead vaccine candidates from each category are highlighted.
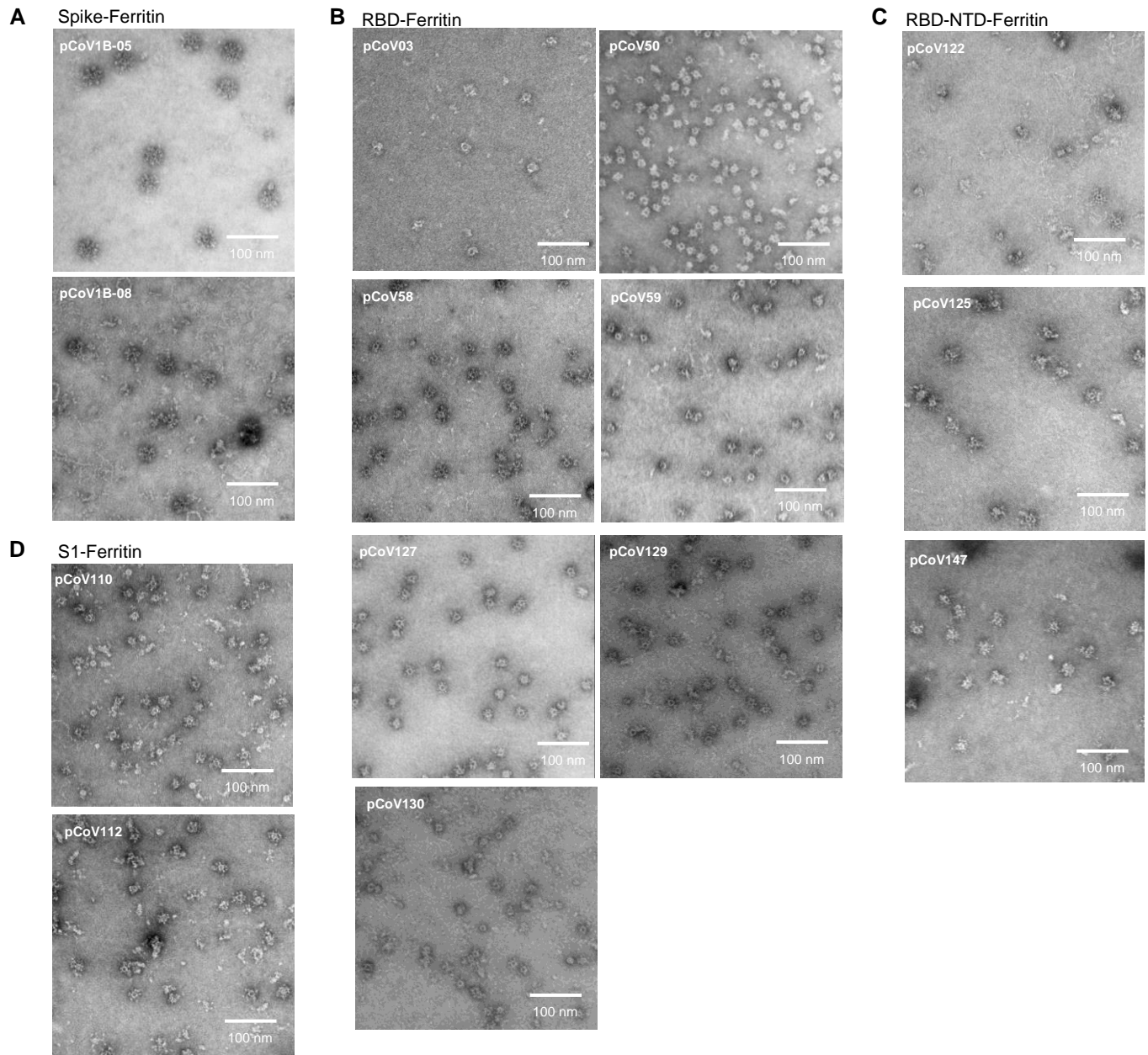
Figure S2. Negative-stain electron microscopy 2D micrographs of SARS-CoV-2 ferritin nanoparticle vaccine candidates, related to Figure 2 and 4.

Negative-stain electron microscopy 2D micrographs. The white scale bars represent 100 nm.
(A) Spike ferritin nanoparticles pCoV1B-05 and pCoV1B-08.
(B) RBD ferritin nanoparticles pCoV03, pCoV50, pCOV58, pCoV59, pCoV127, pCoV129, pCoV130, pCoV131
(C) RBD-NTD ferritin nanoparticles pCoV122, pCoV125, pCoV147
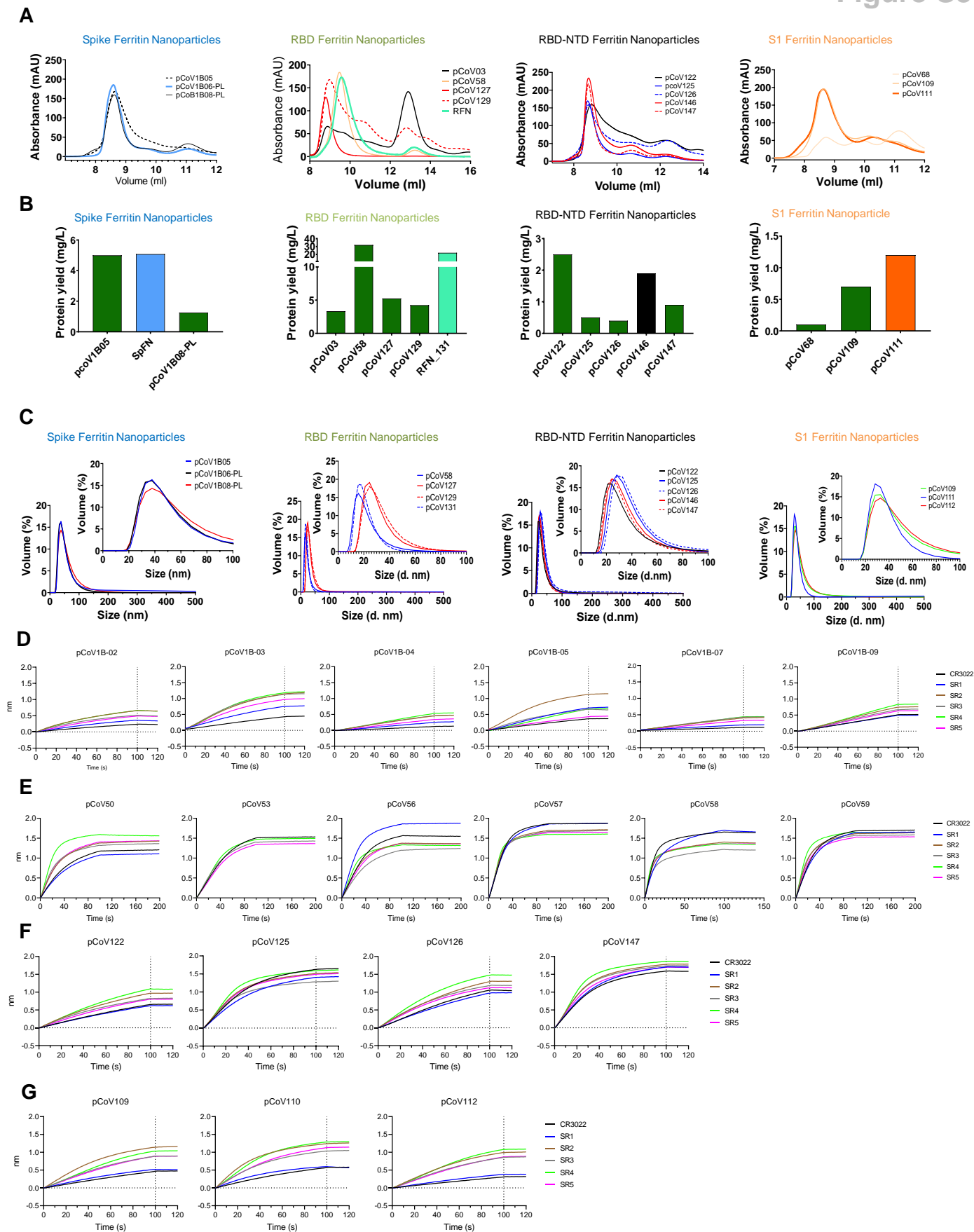(D) S1 ferritin nanoparticle pCoV110 and pCoV112.

Figure S3. Biophysical and antigenic characterization of S-domain ferritin nanoparticle immunogens. Related to Figure 2 and 3.
(A) Size-exclusion chromatography on a Superdex S200 10/300 column of representative SARS-CoV-2 S-based ferritin nanoparticles from the four design categories.
(B) Expression levels (mg/L supernatant) of representative SARS-CoV-2 Spike-based ferritin nanoparticles.
(C) Dynamic light scattering analysis of representative SARS-CoV-2 Spike-based ferritin nanoparticles.
(D) Spike ferritin nanoparticles (E) RBD ferritin, (F) RBD-NTD ferritin and (G) S1 ferritin nanoparticles were assessed for binding to a set of neutralizing antibodies (concentration = 30 μg/ml) by biolayer interferometry.
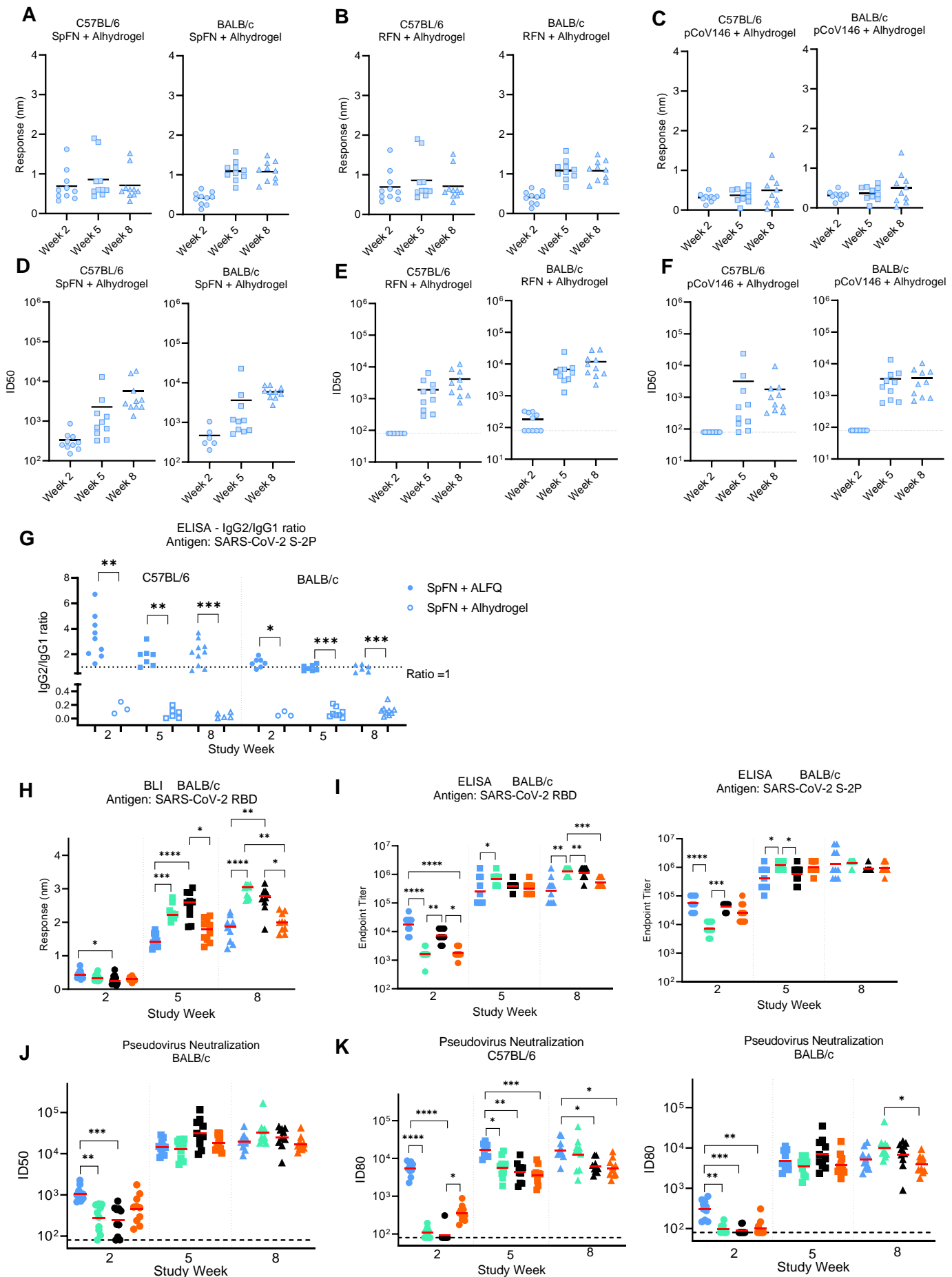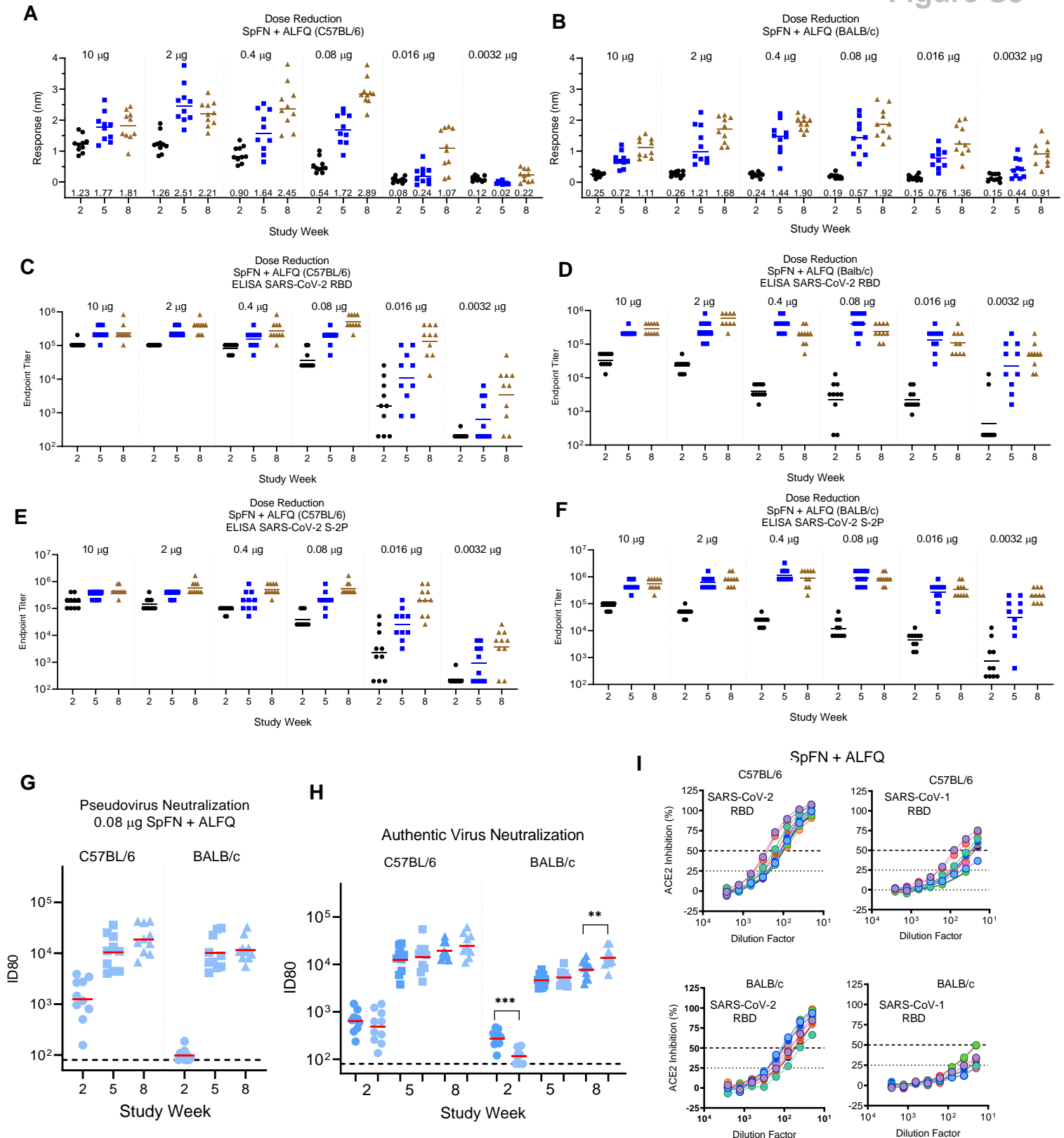
Figure S5

Figure S5 SARS-CoV-2 SpFN vaccine candidate elicits robust binding and neutralizing antibody responses at reduced doses in mice. Related to Figure 5 and 7.

(A) Biolayer interferometry analysis of C57BL/6 and (B) BALB/c mouse sera binding response to SARS-CoV-2 RBD following immunization with reducing doses of SpFN.

(C, E) ELISA analysis of C57BL/6 and (D, F) BALB/c mouse sera binding response to SARS-CoV-2 RBD or S-2P following immunization with reducing doses of SpFN.

(G) SARS-CoV-2 pseudovirus ID80 neutralization titers of mice immunized with 0.08 µg SpFN + ALFQ.

(H) Authentic SARS-CoV-2 virus ID80 neutralization titers of mice immunized with 10 µg (blue) or 0.08 µg (light blue) SpFN + ALFQ. Geometric mean titers for each group and time point are indicated by a horizontal line, n =10. Neutralization titers for the two dose groups at each study time point were compared for statistically significant differences using a Mann-Whitney unpaired two-tailed non-parametric test. The two BALB/c time points that showed differences are indicated by bars. P values <0.001 (***), <0.01 (**).

(I) Mouse sera from study week 10 was analyzed for hACE2 blocking capacity to SARS-CoV-2 RBD (left) or SARS-CoV-1 RBD using a biolayer interferometry assay format.
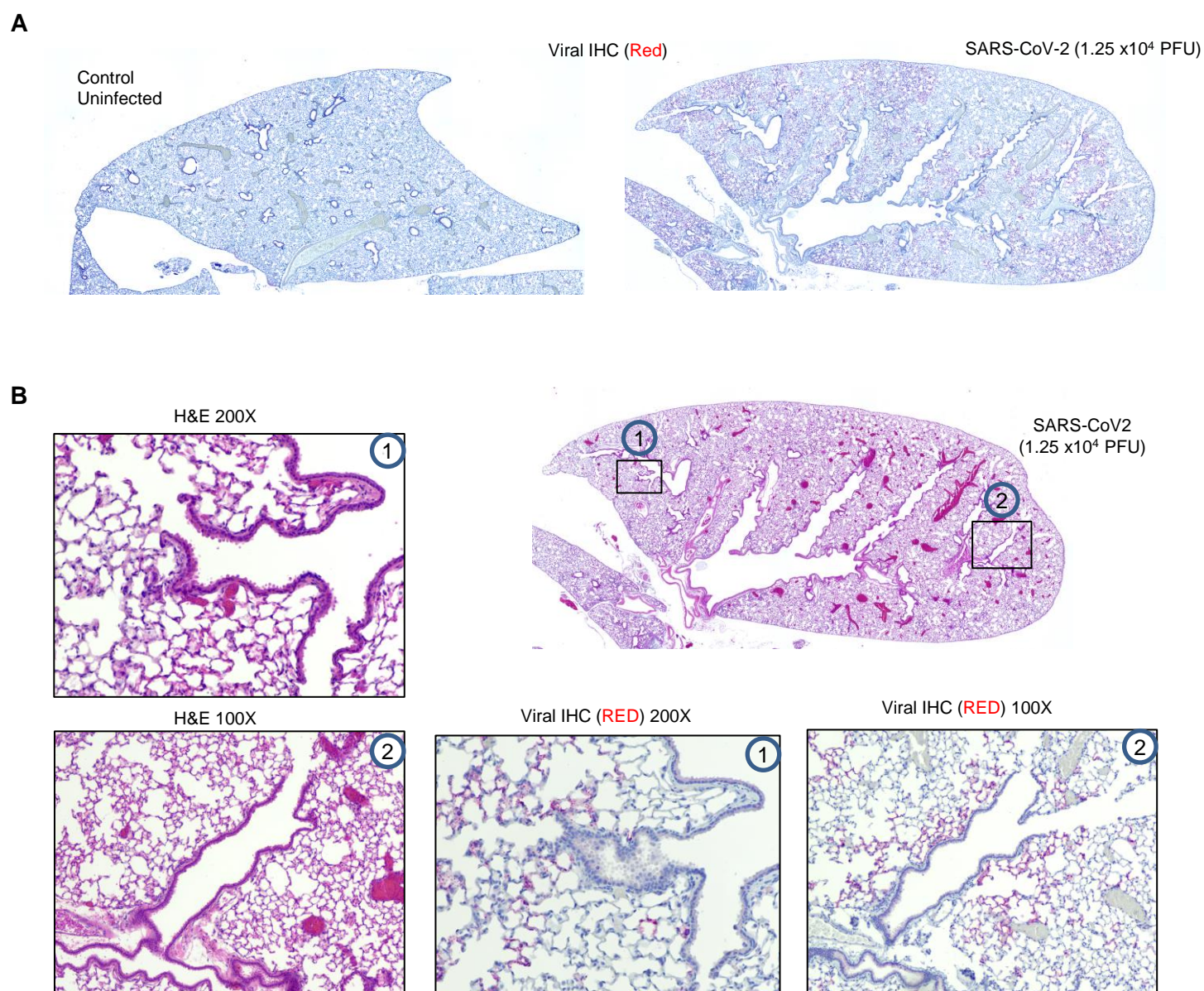
A

Viral IHC (Red)

Control Uninfected

SARS-CoV-2 (1.25 x10^4 PFU)

B

H&E 200X

SARS-CoV2 (1.25 x10^4 PFU)

H&E 100X

Viral IHC (RED) 200X

Viral IHC (RED) 100X

Figure S6 Histopathological analysis of SARS-CoV-2 infection in K18-ACE2 mice. Related to Figure 7

(A, B) Hematoxylin and eosin staining of lung sections from K18-hACE2 mice following intranasal infection with 1.25 x 10^4 PFU SARS-CoV-2. Images show two magnifications. Images are representative of n = 10 per group.